

# RSC Sustainability

Accepted Manuscript

This article can be cited before page numbers have been issued, to do this please use: S. Kumar, S. R. Nayak, M. Balkhandia and I. Chhimpa, *RSC Sustainability*, 2026, DOI: 10.1039/D6SU00083E.



This is an Accepted Manuscript, which has been through the Royal Society of Chemistry peer review process and has been accepted for publication.

Accepted Manuscripts are published online shortly after acceptance, before technical editing, formatting and proof reading. Using this free service, authors can make their results available to the community, in citable form, before we publish the edited article. We will replace this Accepted Manuscript with the edited and formatted Advance Article as soon as it is available.

You can find more information about Accepted Manuscripts in the [Information for Authors](#).

Please note that technical editing may introduce minor changes to the text and/or graphics, which may alter content. The journal's standard [Terms & Conditions](#) and the [Ethical guidelines](#) still apply. In no event shall the Royal Society of Chemistry be held responsible for any errors or omissions in this Accepted Manuscript or any consequences arising from the use of any information it contains.

## Sustainability spotlight statement

View Article Online  
DOI: 10.1039/D6SU00083E

The significant increment in the cumulative installation capacity of solar photovoltaic modules as a source of renewable energy, has led to a tremendous increase in volume of end-of-life (EoL) solar modules, by creating an essential requirement for the solution of sustainable waste management. Our research delivers crucial insights into the substrate dependent charge storage and electrochemical characteristics of recycled silicon derived from end-of-life photovoltaic modules using a less – toxic approach and highlighting the circular economy strategies through the integration of photovoltaic recycling. We have investigated Raman effect, revealing vibrational modes of crystalline silicon along with the Si-O stretching mode that indicated the partial surface oxidation of silicon. Furthermore, the electrodes were prepared from recycled silicon powder over different substrates and their electrochemical characterizations further validate our findings.



# Recycling of solar cells recovered from waste panels into efficient silicon-based composite electrodes for energy storage applications

View Article Online  
DOI: 10.1039/C6SU00083E

Soumya Ranjan Nayak<sup>1,2</sup>, Manisha Balkhandia<sup>1,2</sup>, Imran Chhimpia<sup>1,2</sup>, Sushil Kumar<sup>1,2</sup>

<sup>1</sup>CSIR- National Physical Laboratory, Dr. K.S. Krishnan Marg, New Delhi 110012, India

<sup>2</sup>Academy of Scientific and Innovative Research (AcSIR), Ghaziabad – 201002, India

\*E-mail of Corresponding Author -: [skumar@nplindia.org](mailto:skumar@nplindia.org)

With significant increment in the cumulative installation capacity of solar photovoltaic modules as a source of renewable energy, has led to a tremendous increase in volume of end-of-life (EoL) solar modules, by creating an essential requirement for the solution of sustainable waste management. In this work, an eco-friendly and less toxic recycling process has been developed to recover the silicon and native silica (SiO<sub>2</sub>) from discarded crystalline silicon solar cells for their use as a functional electrode material for different faradaic energy applications. The recovered materials were chemically treated and employed to fabricate slurry-coated electrodes over copper foil. This recovered silicon was also deposited over various substrates, including Indium Tin Oxide (ITO) coated glass and graphite sheet to examine how the substrates affect the overall charge-storage reaction mechanism. The recycled material was structurally characterized using XPS, XRD, XRF and Raman spectroscopy, whereas morphological properties were analysed by employing TEM, SEM, EDAX and AFM. The thermal analysis was carried out using TGA to evaluate the thermal stability and compositional changes of the recycled silicon powder. The surface properties were also analysed using BET to determine the surface area and porosity of the powder. The electrochemical characterizations including CV, EIS and GCD were performed on the prepared electrodes. The study presents an eco-friendly solution by integrating recycled photovoltaic waste into electrode materials in Li-ion electrochemical systems with an emphasis on substrate dependent faradaic charge storage behaviour and further highlights substrate dependent charge storage with electrodes formed on ITO and graphite sheets showing different charge-storage characteristics. The prepared electrodes over Cu foil, ITO and graphite sheet exhibited specific capacitance values of 143.23 Fg<sup>-1</sup>, 30.53 Fg<sup>-1</sup> and 163.92 Fg<sup>-1</sup> respectively.

## 1 Introduction

In recent decades, the installation of solar photovoltaic (PV) <sup>1,2</sup> capacity is continuously increasing, resulting in the substantial accumulation of large quantity of solar waste being



generated that requires urgent end of life (EoL) <sup>3,4,5</sup> solutions. This solar waste flux makes PV industry susceptible to an unprecedented waste management challenge.<sup>6,7</sup> As per International Renewable Energy Agency (IRENA) report, world renewable energy capacity amounted to 4448 GW at the end of 2024.<sup>8</sup> Solar accounted for the largest share (~ nearly 42%) of the global total, with a capacity of 1865 GW.<sup>9</sup> India's current solar power capacity is  $\square$  133 GW till the end of 2025.<sup>10</sup> However, as photovoltaic panels installed around the late 1990s and early 2000s already reached their end of life due to limited lifespan of 25 to 30 years, generating large volumes of solar PV waste. This growing challenge highlights the urgent need for effective recycling strategies and policy frameworks to manage end-of-life solar panels thereby ensuring a sustainable energy cycle.<sup>11,12</sup> The end-of-life pressure, combined with manufacturing residues such as kerf and cutting waste generated during wafering and module fabrication, presents both an environmental challenge and a valuable resource recovery opportunity.<sup>13,14</sup> Silicon recovered from PV wafers represents a high-value material for reuse due to its intrinsic electrochemical properties that far exceeds those of conventional graphite anodes used in lithium-ion batteries (LIBs).<sup>15,16</sup> Silicon possesses a theoretical specific capacity of around 4,200 mAh g<sup>-1</sup> which is more than ten times higher than graphite's 372 mAh g<sup>-1</sup>, making it an exceptionally attractive high-capacity anode precursor.<sup>17,18</sup> Recent studies demonstrate that nano-structured or processed PV silicon can be converted into active anode materials for lithium-ion batteries, providing direct value addition from end-of-life modules.<sup>7,19</sup> Moreover, the SiO<sub>x</sub>/SiO<sub>2</sub> content naturally present in recycled PV silicon can be tuned to form Si-SiO<sub>x</sub> hybrid phases that contribute an inert buffering matrix during lithiation, an effect exploited in several recent anode designs to enhance electrochemical stability.<sup>20,21</sup> Also, silicon being one of the most abundant elements (second highest) in the Earth's crust offers high availability and environmental sustainability as an anode material for Li-ion batteries.<sup>22,23</sup> When Si used as an active material in lithium-ion batteries, it undergoes significant volume changes during repeated lithiation and de-lithiation due to its intrinsic properties.<sup>24</sup> Several progresses have been achieved in silicon anode development through improved synthesis strategies, including template-based routes, chemical vapor deposition (CVD), sol-gel, hydrothermal, spray-drying, and self-assembly methods. These approaches enable precise control over nanosheet size and structure, while surface engineering and composite design further enhance electrochemical performance and battery compatibility. Compositing carbon materials with Si helps accommodate the tension within the electrodes and enhance their conductivity.<sup>25</sup> Zhang et al.,<sup>26</sup> fabricated carbon nanotubes (CNT)-interconnected SiO<sub>x</sub>/C@C spherical structures with an

View Article Online  
DOI: 10.1039/D6SU00083E

RSC Sustainability Accepted Manuscript



outer carbon layer, achieving a high reversible capacity of 857.7 mA h g<sup>-1</sup> at 0.1 A g<sup>-1</sup>, cycling stability 333.3 mA h g<sup>-1</sup> at 0.1 A g<sup>-1</sup>, and excellent rate capability 333.3 mA h g<sup>-1</sup> at 10 A g<sup>-1</sup>. Similarly, Fan et al.,<sup>27</sup> reported the encapsulation of carbon-coated Si nanoparticles within a CNT-reinforced carbon framework derived from ZIF-67, delivering a stable capacity of 680 mA h g<sup>-1</sup> after 1000 cycles at a current density of 1 A g<sup>-1</sup>. While combining silicon nanoparticles with carbon nanotubes improves electrode performance, significant issues still exist. Insufficient bonding at the Si–C interface can cause structural failure during repeated cycling.<sup>28</sup> Therefore, there is a strong need for simple, economical fabrication strategies that can deliver Si/C electrodes with high conductivity and durable cycle stability. The present work explores the electrochemical performance of Si-CNT electrodes developed using silicon derived from waste PV modules giving second life to the embedded silicon post EoL. The novelty of the work lies in the development of purification and composite fabrication process that yields Si-CNT electrodes with reasonable cycling stability, systematic investigation of recycled PV silicon quality and its impact on CNT-mediated electrochemical performance. The research demonstrated that recycled silicon from solar panel waste can achieve performance of stability for about 500 cycles. Therefore, the present research contributes to the dual goals for advanced next-generation energy storage technologies. First, the research recovers valuable silicon from waste PV panels and second, the reclaimed silicon used as an electrode material in Li-ion based electrochemical systems<sup>29</sup> to promote environmental sustainability in the battery materials supply chain.

In this work it is proposed to prepare the electrode materials using silicon solar cell waste and the observed electrochemical behaviour in Li-ion environment along with the characteristics of the composite material over other conducting substrates like ITO and graphite sheet. In the first step, the recycled solar cell scraps are powdered using ball milling to obtain micron size particles. The advantages of this size particles are that they provide lower specific surface area and greater volumetric capacity. The recycled silicon powder is then treated with NaOH and HCl to remove the impurities. This powder along with a conductive additive and a binder formed a composite slurry, which is deposited over different substrates to observe the behaviour of the active material silicon. Different spectroscopic analysis along with the X-ray diffraction spectroscopy (XRD), scanning electron microscopy (SEM), energy dispersive X-ray spectroscopy (EDAX) and Raman spectroscopy of both the recycled material and the slurry coated electrode were done. Transmission electron microscopy (TEM) of the resulted silicon powder after chemical treatment was done to investigate the morphology and microstructure



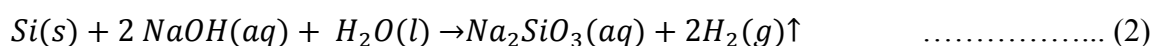
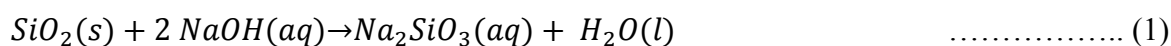
of the recycled silicon powder, which provides detailed information about the crystallinity through high resolution imaging and SAED pattern analysis. Also, Thermogravimetric analysis (TGA) along with Differential Scanning Calorimetry (DSC) and Brunauer–Emmett–Teller Analysis (BET) of the chemically treated powder was done to evaluate the thermal stability and to determine the surface area as well as porosity of the powder respectively. The atomic force microscopy (AFM) and X-ray photoelectron spectroscopy (XPS) was performed only to know the surface topography and electronic state of the elements present in the recycled powder. In addition to this, electrochemical characterizations, including cyclic voltammetry (CV), Electrochemical impedance spectroscopy (EIS) and galvanometric charge – discharge (GCD) were also done on the prepared electrodes.

## 2 Experimental Section

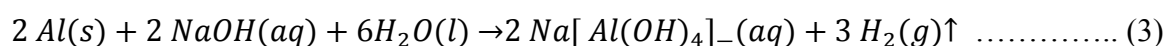
### 2.1 Recycling Process of Silicon Solar module

The waste silicon solar photovoltaic modules are first disassembled manually to separate the aluminium frames. After the removal of aluminium frames, the waste solar cells attached between both the front and back sides of Ethyl Vinyl Acetate (EVA) layers and back-sheet are then subjected to thermal treatment at an optimized temperature of 480<sup>0</sup> C. This controlled thermal treatment resulted in the effective removal of EVA encapsulation layers, back-sheets and glass fragments along with the silicon solar cell scraps. The individual silicon solar cell scraps were collected in a petri dish, then crushed and made into fine powder using ball milling process at 450 rpm for 6 hours. This resulting fine powder primarily consists of Si, Ag and Al. This powder sample was then treated with aqueous NaOH solution under continuous stirring.

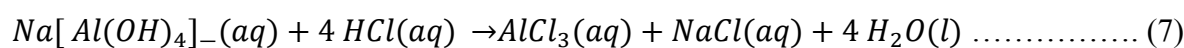
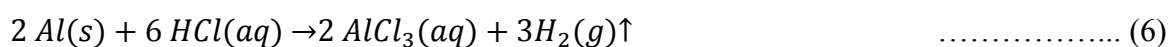
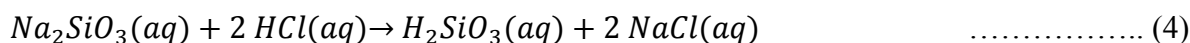
In this alkaline environment, surface oxides associated with the solar cell waste were partially dissolved by forming soluble sodium silicate, while metallic silicon and other insoluble components remained undissolved.



The resulting mixture underwent filtration, and the solid residue that remained on the filter paper was collected. This collected solid material was then subjected to multiple rinses with deionized water (DI water) in order to ensure the removal of any residual soluble sodium-containing compounds.



After the washing procedure, the precipitate was subjected to treatment with HCl solution. This process facilitated the transformation of metallic and other inorganic impurities into their respective chlorides, which intensifies their solubility.<sup>30</sup> Along with this simultaneously the acidification promoted the silica formation by precipitating the surplus silicate compounds that were embedded within the solid matrix. This obtained suspension was then subjected to filtration, and the recovered solid was washed repeatedly with DI water to leach out chloride ions. The final product was dried at varied temperature for further analysis.



The schematic of the steps of recovery process of silicon and silica powder from waste PV modules and its application in electrode fabrication is shown in figure 1.



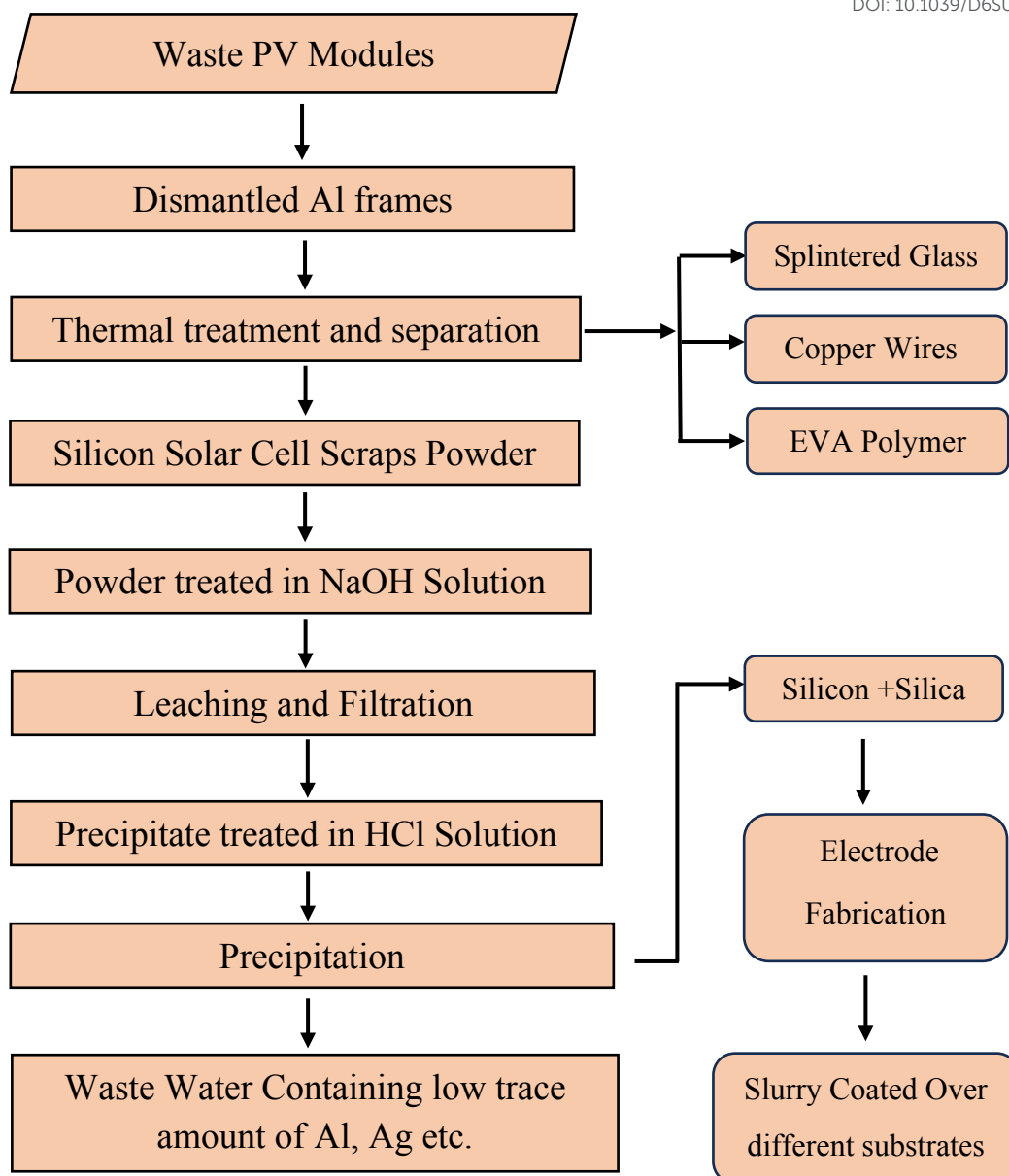


Fig. 1 The flowchart of the of the recovery process of silicon and silica powder from waste photovoltaic modules and its subsequent application in electrode fabrication.



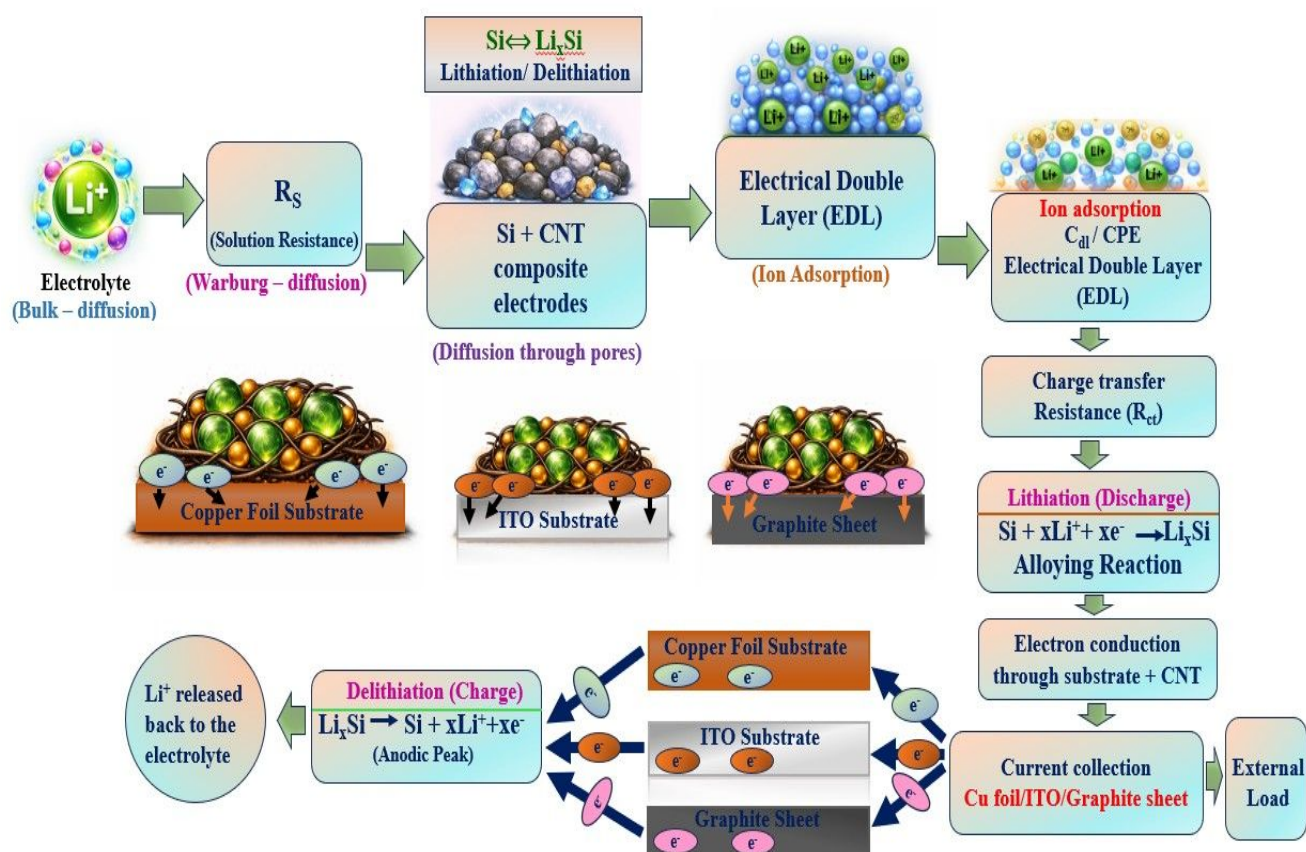


Fig. 2 Flowchart illustrating the charge transfer process

## 2.2 Fabrication of electrodes using the recovered powder as the active material

The chemically recovered powder which consisted of both Si and SiO<sub>2</sub> was utilized as the essential active material for the electrode fabrication. For the fabrication of the electrodes, the recycled powder was integrated with carbon nanotubes (CNTs) as conductive additive, Polyvinylidene fluoride (PVDF) as a binder, N-methyl-2-pyrrolidone (NMP) as the solvent medium in the ratio of 80:10:10 to prepare the slurry. This prepared slurry was then coated over copper foil, ITO and graphite sheet which acted as current collectors. The coated films over copper foil, ITO and graphite sheet were dried in a vacuum oven at around 90<sup>o</sup> C – 100<sup>o</sup> C to eradicate excess solvent and facilitate adhesion between the substrate and the binder. The electro-chemical performance of the fabricated electrodes was evaluated using the electrolyte composed of 1 M LiClO<sub>4</sub> mixed with Propylene carbonate (PC). Here Ag/Ag<sup>+</sup> was used as reference electrode and Au was used as counter electrode.



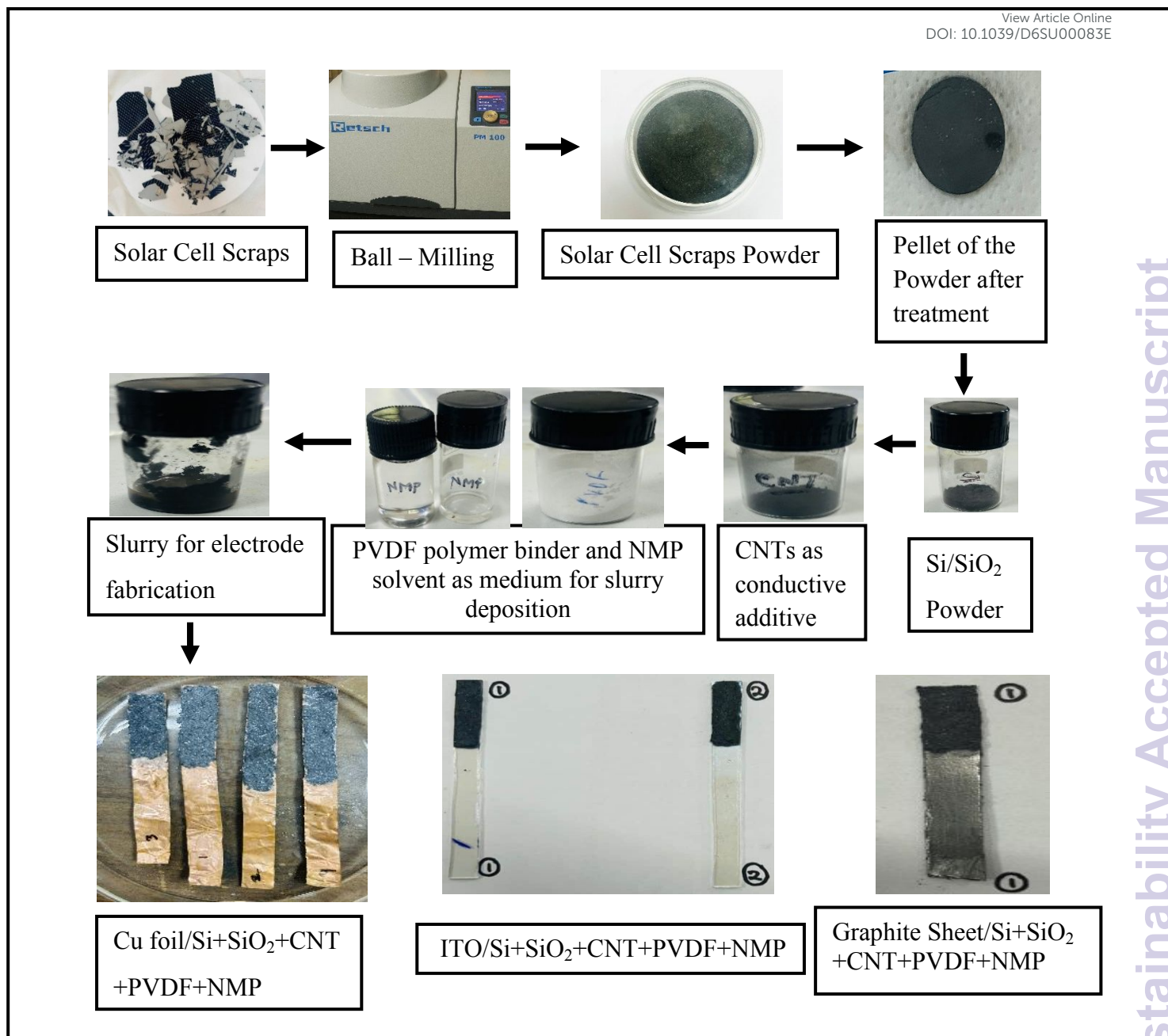


Fig. 3 Complete Steps for the fabrication of electrodes using recycled silicon solar cell powder

### 2.3 Recovery of Silicon Powder

A cut solar cell module of weight 500 gm was put under thermal treatment to get solar cell pieces along with glass and copper wires. The solar cell pieces were then separated from other recovered materials and crushed into powder using ball-milling apparatus at 450 rpm for 6 hours with an interval of 10 minutes. The weight of the crushed solar cell powder was found to be 12.32 gm. Out of this quantity of recycled powder 12 gm was taken and divided into 3 batches of 4 gm each and then treated with NaOH and HCl in a molar ratio of 1:1, 1:1.25 and



1:1.5 respectively. The recovered silicon powder after the chemical treatment with NaOH and HCl was found to be 3.85 gm, 3.91 gm and 3.82 gm respectively. Therefore, the recovery percentage was observed highest for the 1:1.25 molar ratio which was about 97.75%. This is estimated based on work done by D. Sah et al.<sup>31</sup>

### 3 Results and Discussion

#### 3.1. X-ray diffraction Spectroscopy

The X-ray diffraction pattern of the recycled solar cell scraps powder was recorded within the range from  $10^\circ$  to  $80^\circ$  on a  $2\theta$  scale in Fig. 4A using Rigaku Mini Flex II X-ray diffractometer operating with Cu-  $K_\alpha$  radiation of wavelength  $1.54 \text{ \AA}$ . The highly intense diffraction peak was appeared at  $2\theta \approx 28.6^\circ$ , which correspond to the (111) plane of crystalline silicon. This intense peak was appeared primarily due to the diamond cubic crystal structure of silicon, which confirmed the retention of its crystalline form in the recycling process. The additional peaks located at angles  $47.5^\circ$ ,  $56.2^\circ$ ,  $69.2^\circ$  and  $76.5^\circ$  were assigned to the (220), (311), (400) and (331) planes, which further confirms the presence of crystalline silicon. The X-ray diffraction pattern also show the evidence of presence of metallic residues like aluminium (Al) and silver (Ag). The diffraction peaks appeared at  $2\theta \approx 38.6^\circ$ ,  $2\theta \approx 65.1^\circ$  and  $2\theta \approx 78.3^\circ$  were attributed to the (111), (220) and (311) planes of aluminium, which originated from the back-contact layer of silicon solar cell. The only peak of silver (Ag) was observed in this x-ray diffraction pattern at around  $2\theta \approx 44.8^\circ$  which was indexed to the (200) plane and comes from the front metal grid of silicon solar cell.

The crystalline properties of the recovered powder, obtained from the solar cell scraps after consecutive treatment with NaOH and HCl was examined using X-ray diffraction (XRD) technique. The diffraction pattern as shown in Fig. 4B displayed sharp and well-defined diffraction peaks, which confirms the presence of multiple crystalline phases within the recycled powder sample. The major diffraction peaks observed at around  $2\theta \approx 28.4^\circ$ ,  $47.3^\circ$ ,  $56.1^\circ$ ,  $69.1^\circ$  and  $76.2^\circ$  corresponds to the (111), (220), (311), (400) and (331) crystal planes of silicon. Apart from the silicon peaks, an additional peak at around  $26.6^\circ$  corresponds to the (102) plane of silicon dioxide ( $\text{SiO}_2$ ), indicating that during chemical treatment process silicon surfaces experienced partial oxidation. The presence of  $\text{SiO}_2$  is because of the interaction with aqueous environments generally facilitate the formation of thin oxide layers over silicon particles. Thus, the X-ray diffraction patterns confirmed that recycled powder mainly consists of crystalline silicon along with small contributions from silicon oxide ( $\text{SiO}_2$ ). The co-existence



of crystalline silicon with minor secondary phase like SiO<sub>2</sub> demonstrates that the chemical treatment efficiently Silicon (Si), which coincides with the standard JCPDS card no. 00-027-1402. The strong intensity peak corresponding to the (111) plane shows the preferred orientation of the recovered and successfully separated silicon and along with that preserved its crystalline nature.

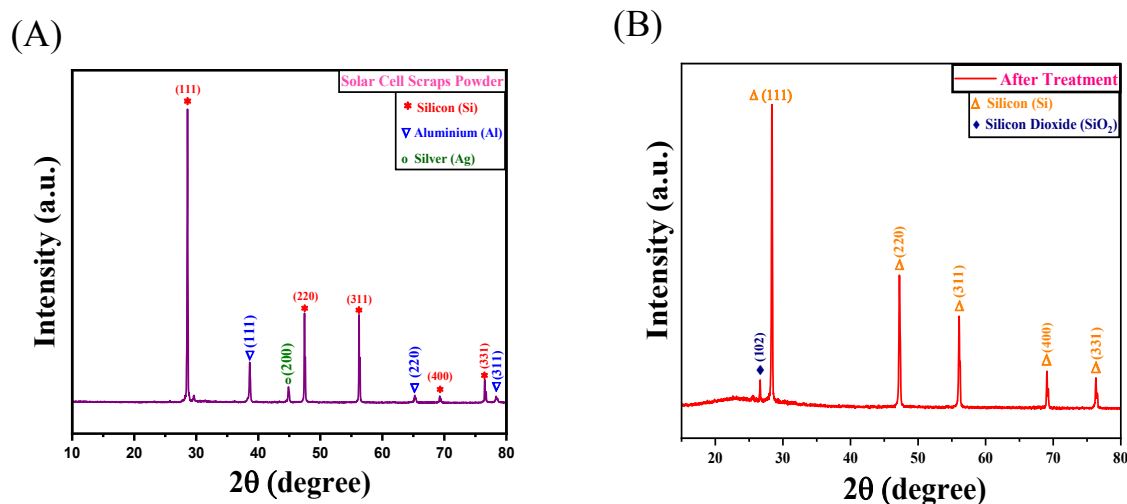
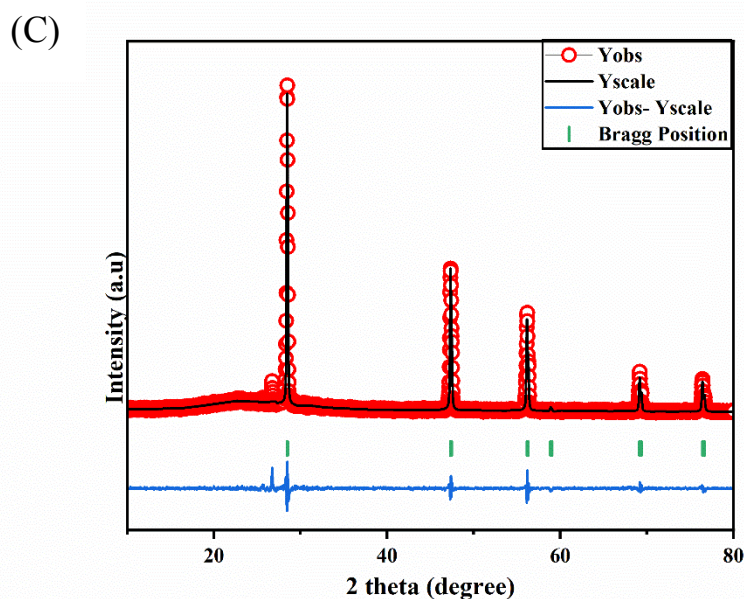


Fig. 4 XRD plots of the recycled solar cell scraps powder (A) before chemical treatment , (B) after chemical treatment. The powder sample without chemical treatment exhibits characteristic diffraction peaks of crystalline silicon along with the impurity phases of aluminium (Al) and silver (Ag). The XRD pattern of the powder sample after chemical treatment in (B) is primarily composed of silicon peaks along with the presence of silicon dioxide (SiO<sub>2</sub>) due to the partial oxidation, while the elimination of impurities confirms the efficiency of the treatment and (C) Rietveld refinement of the X-ray diffraction pattern of chemically treated recycled silicon powder. The experimentally observed intensities in red circles are in good agreement with the calculated patterns that are in black solid lines showing good quality fitting. The vertical green lines represent the Bragg reflection positions corresponding to the crystalline silicon.

The crystallinity index (CI) of the prepared silicon powder sample after chemical treatment is found to be 48% from its XRD plot. Further to determine concentration of Si on the crystallite growth, we have calculated crystallite size and lattice strain produced in the lattice using the well-known Williamson – Hall equation :

$$\beta \cos \theta = \frac{K\lambda}{D} + 4\epsilon \sin \theta \quad \dots \dots \dots (8)$$





Where  $\beta$  is the FWHM that corresponds to each peak in XRD data measured in radians,  $\theta$  is the diffraction angle in radians,  $K$  is the shape factor considered to be equal to 0.9 for our sample,  $\lambda$  is the wavelength of X-rays (Cu  $K_{\alpha}$  source in our case),  $D$  is the crystallite size, and  $\epsilon$  is the lattice strain.

The crystallite size  $D$  is calculated to be 67.28 nm and the lattice strain  $\epsilon$  is found to be  $9.28 \times 10^{-4}$  from the Williamson – Hall equation.

The Rietveld Refinement analysis of the chemically treated recycled silicon powder is done and the parameters are represented in the Table 1.

Table 1.

Rietveld Refinement details of the recycled silicon powder sample after chemical treatment

$R_p$	$R_{wp}$	$R_{ep}$	$\chi^2$	$a=b=c$ (Å)
35.8	25.8	12.99	3.93	5.426



### 3.2. FESEM- EDAX analysis

The Fig. 5 is the cross-sectional Field Emission Scanning Electron Microscopy (FESEM) image of a crystalline silicon solar module which explains the multilayer structure of it. The glass was removed from the sample used for cross – sectional FESEM. As clearly labelled in the micrographs below, the back-sheet, subsequent EVA encapsulant, the core silicon wafers and a second EVA layer arranged sequentially from bottom to top. The sheet protects the inner layers from external stress, while the EVA acts as an encapsulant as well as protective and optical coupling materials. They securely hold the silicon wafers back- within them where energy conversion occurs.

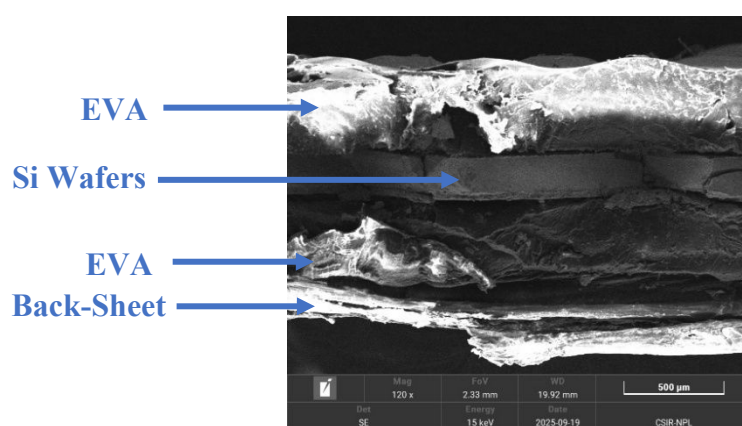


**Fig. 5 Cross – sectional FESEM image of a crystalline silicon solar module after the removal of glass highlighting the presence of the silicon wafer pieces within the front and back EVA layers along with the back-sheet layer beneath it.**

For understanding of the surface morphology and distribution of impurities in the crushed powder sample, it was characterized through the field emission scanning electron microscopy (FESEM) and energy dispersive x-ray spectroscopy (EDAX). The Fig. 6A displayed a heterogeneous mixture of non-uniform particle morphology with irregular geometries, which is due to the crushing and material breakdown process during recycling. The microstructure consisted of a combination of fine small grains along with larger thin sheet like particles, which indicates the presence of silicon-abundant domains as well as the residual surface layers.

The EDAX spectrum in Fig. S1A and EDAX data in Fig. 6B has confirmed that the recovered silicon solar cell scraps powder sample was composed of silicon (Si) which is nearly 71.09% by weight and 65.88% by atomic percentage. The second major component present in the powder sample is aluminium with a weight percentage of 19.04% and an atomic percentage of 18.37%. The 9.64% weight percentage and 15.69% atomic percentage of oxygen highlight



the presence of oxide phases might be associated with either silicon or aluminium. In addition to that, the presence of very small amount of silver having 0.22% (in weight %) and 0.05% (in atomic %) indicates a very little amount of metallic residue arise from front contact electrodes. No hazardous elements like lead (Pb) were observed in the EDAX data.<sup>32</sup> Therefore, it can be concluded from here that the recycled powder is primary made of crystalline silicon with metallic impurities like Ag and Al, which comes from the electrode and back contact layers.

The crushed silicon solar cell powder is then treated firstly with NaOH and the precipitate collected from this process is then treated secondly with HCl. The FESEM image in the Fig. 6C shows the presence of unevenly shaped and non-uniform particles with etched and irregular surfaces. The treatment with NaOH efficiently etched the silicon resulting micro-size grains with fine particles. Following this step, the chemical reaction with HCl produces a mixture of silicon flakes and more finer particles. The presence of surface roughness is observed because of the SiO<sub>2</sub> content. The Fig. S1B shows the EDAX spectrum and the Fig. 6D provides the EDAX data which highlights the changes occurred in the elemental composition after the two-step chemical treatment process. From the EDAX data it is observed that the treated powder consists of 53.76 wt.% silicon along with contributing 67.09 as at.% of the all-total detected elements. The noticeable quantity of oxygen is either due to the formation of SiO<sub>2</sub> layer which arises because of the HCl induced precipitation, from the sodium silicate formed during the alkaline treatment or due to the oxidation of etched silicon surfaces. A negligible amount of Al (□ 1.69 wt.%) is detected, which is primarily come from the back contact of the silicon solar cell during the recycling process. As compared to the EDAX data of the powder before chemical treatment, the Ag impurities are removed after the chemical treatment process. Therefore, the SEM microstructural image and the EDAX data ensures that this recycling process produces a Si/SiO<sub>2</sub> powder. This surface texture and oxide presence will help in providing better performance in electrode fabrication.



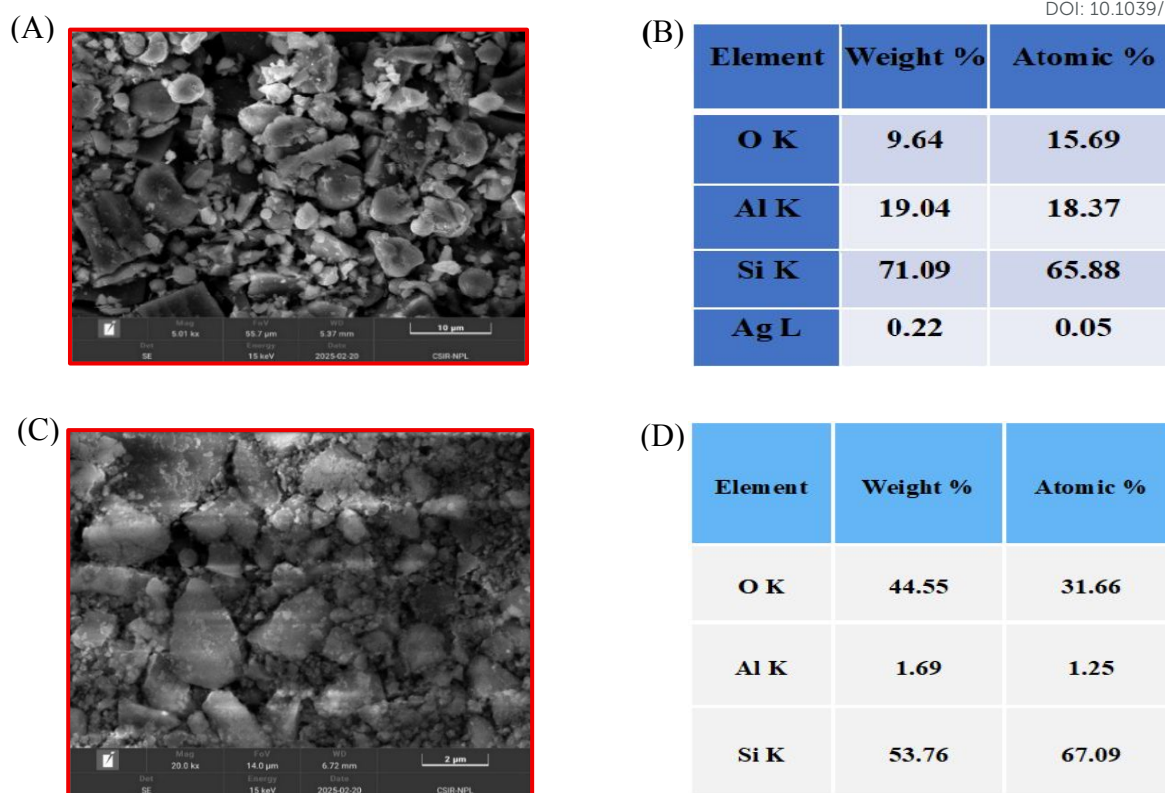


Fig. 6 (A) FESEM image of crushed silicon solar cell scraps powder before chemical treatment showing irregularly shaped agglomerated particles and non-uniform surface morphology with its corresponding (B) EDAX analysis confirming the presence of silicon as the primary element along with appreciable content of Al and O along with traces of Ag, (C) FESEM image of the chemically treated solar cell scraps powder displaying relatively cleaner surface morphology along with reduced agglomeration, suggesting the removal of impurities, with its corresponding (D) EDAX analysis indicating reduction in wt.% of Si and Al along with a higher content of O formation due to the presence of  $\text{SiO}_2$  after the chemical treatment.

### 3.3. Raman Spectroscopy analysis

Fig. 7A shows the Raman spectra of the recycled silicon solar cell scraps powder after chemical treatment with NaOH and HCl. The spectrum exhibits a distinct and intense peak at around  $516 \text{ cm}^{-1}$ , which signifies the first order optical phonon vibration mode of crystalline silicon. This strong and distinct peak indicates that the recycled powder retains mainly its crystalline nature after the chemical treatment processes. The spectrum also shows a small band at around  $295 \text{ cm}^{-1}$ , that corresponds to the higher order phonon interactions in silicon.<sup>33</sup> In addition to this, a broad peak near  $960 \text{ cm}^{-1}$  relates to the Si-O stretching that indicates the partial surface



oxidation of silicon because of the chemical treatment. After the chemical treatment process, the recovered powder was subjected to high temperature annealing at 1500<sup>o</sup> C in a vacuum tube furnace under an inert atmosphere and the Raman spectrum of this powder is shown in Fig. 7B. This spectrum exhibits a sharp and intense peak at around 524 cm<sup>-1</sup>, which again shows the characteristic feature of the first order optical phonon mode of crystalline silicon. This post annealed Raman spectra shows more intense and slightly shifted peak which signifies better crystallinity and reduction in crystal defects. The weaker band at around 307 cm<sup>-1</sup> remains present, which corresponds to the higher order phonon interactions in silicon. Moreover, a broad band at around 963 cm<sup>-1</sup> originates from Si-O stretching vibrations signifying a small contribution from oxide phases. These results confirm that the vacuum furnace annealing

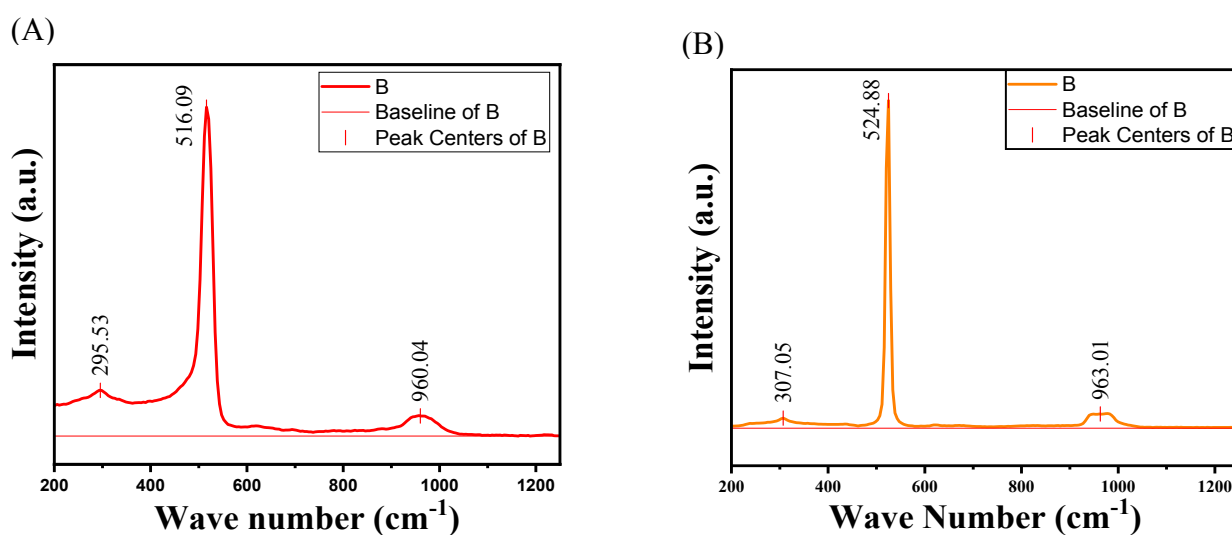


Fig. 7 Raman spectroscopy plot of recycled silicon powder (A) before annealing, shows a broadened Si peak at  $\square$  516.09 cm<sup>-1</sup> signifying structural disorder and phonon confinement effects. (B) Raman spectrum after annealing highlights a sharper and more intense peak at  $\square$  524.8 cm<sup>-1</sup> along with reduced broadening that confirms the enhancement in crystallinity and defect reduction.

improves crystallinity of the recycled silicon powder, which increases its suitability for electrode fabrication.

### 3.4. X-ray photo electron spectroscopy analysis

The Fig. 8 shows the x-ray photoelectron spectroscopy plot, which investigates the chemical composition and electronic states of Silicon 2p core level spectrum of the recycled powder. This spectrum produces distinct peaks of both elemental silicon (Si) and silicon dioxide (SiO<sub>2</sub>), which confirms the existence of both of them within the chemically treated sample. Here as



shown in the Fig. 8, two characteristic doublets were observed in the spectrum which signifies the spin-orbit coupling of Si 2p core level electrons. The lower binding energy peaks at around 99.0 eV to 100.0 eV corresponds to the Si 2p<sub>3/2</sub> and Si 2p<sub>1/2</sub> states of crystalline silicon and the peaks corresponding to higher binding energy approximately at around 103.0 eV to 104.0 eV indicates the Si 2p<sub>3/2</sub> and Si 2p<sub>1/2</sub> states of oxidized silicon, representing +4 oxidation state of Silicon.<sup>34</sup> The presence of these silicon oxide peaks highlights the surface oxidation of the recycled silicon in the chemical treatment process. The fitted curve (in red) denoted as peak sum matches closely with the experimental intensity spectrum.

The strong intensity of the oxide-related peaks suggests that a substantial portion of the powder surface is oxidized. The existence of both Si and SiO<sub>2</sub> peaks indicate that the chemical treatments using NaOH and HCl partially remove native surface oxide but also enhanced oxidation, producing a composite of both elemental Si and SiO<sub>2</sub>.

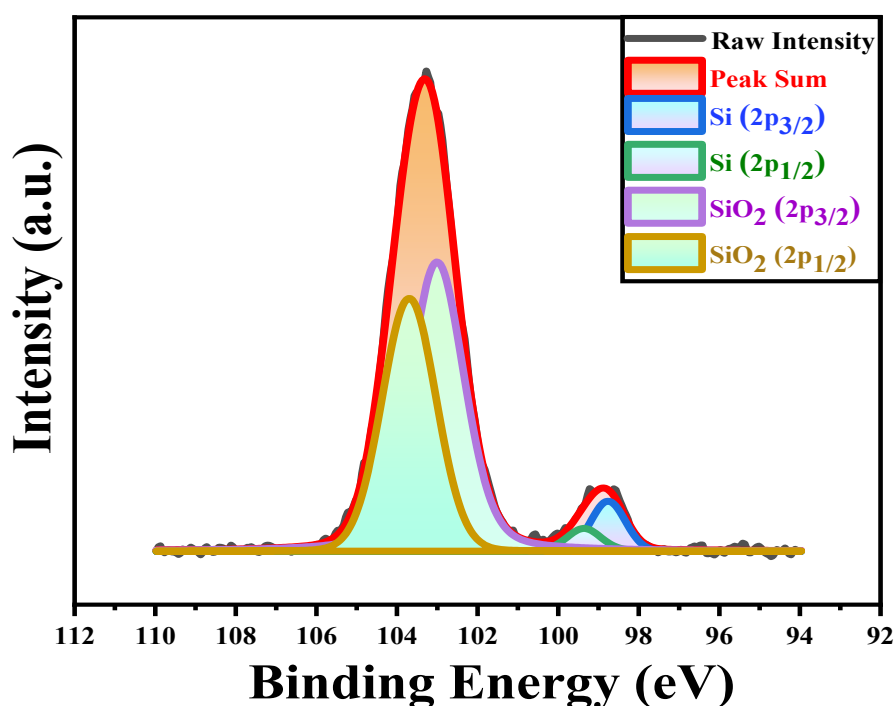


Fig. 8 X-ray Photoelectron Spectroscopy plot of the chemically treated silicon powder showing the deconvoluted Si 2p region. The raw intensity (in black) and fitted peak sum (in red) are highlighted along with the peaks of the individual components corresponding to elemental silicon (Si 2p<sub>3/2</sub> and Si 2p<sub>1/2</sub>) and oxidized silicon contributions (SiO<sub>2</sub> 2p<sub>3/2</sub> and SiO<sub>2</sub> 2p<sub>1/2</sub>). The spectrum is dominated by Si 2p contributions confirming the presence of elemental silicon, whereas the presence of SiO<sub>2</sub> related components indicate the partial surface oxidation of the recovered powder.



### 3.4. Atomic Force Microscopy image analysis

View Article Online  
DOI: 10.1039/D6SU00083E

The surface topography of the recycled silicon solar cell scraps powder after the chemical treatment with NaOH and HCl was studied by atomic force microscopy (AFM). This image shows a heterogeneous surface consisting of densely packed fine particles present across the whole mapped surface. The height of the scale bar indicates about a broad vertical profile, which shows the presence of both small granules and large agglomerated particles after the chemical treatment of the powder sample.<sup>35</sup> The surface morphology shows the presence of both brighter and darker regions composed of silicon and silicon oxide containing particles due to the removal of surface layers during chemical etching. The existence of sharp rises and deep depressions results a highly distinct rough nano-scale surface, which is good for lithium-ion storage as it helps in better electrolyte penetration along with the improvement in the charge-transfer kinetics across the electrode – electrolyte interface.

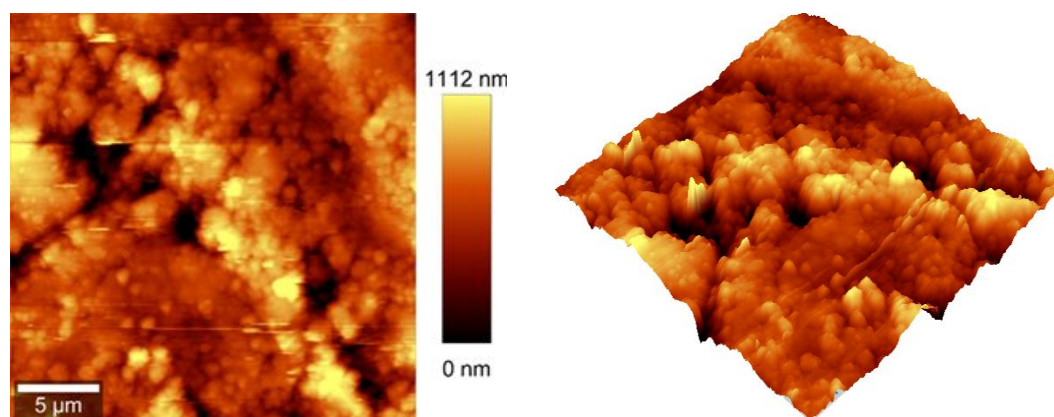


Fig. 9 AFM image analysis of recycled silicon powder after chemical treatment (a) 2D- image illustrates the surface morphology revealing agglomerated particle features with distinct surface roughness. The height of the surface varies up to 1112 nm. (b) The 3D topographical image shows the surface texture and height distribution, confirming the presence of irregularly distributed clusters.

### 3.5. Transmission Electron Microscopy and SAED pattern analysis

The microstructures of the recycled silicon powder after chemical treatment were analysed using transmission electron microscopy. The bright field TEM image in Fig. 10A shows irregular sheet like structures having sizes within the sub-micron range, indicating the aggregation of finer particles. The corresponding high-resolution TEM image observed in Fig. 10B exhibits distinct lattice fringes that confirm the crystalline nature of silicon. The limited irregularity and discontinuity in the crystal planes suggest the formation of structural defects



during the chemical treatment process. In addition to that, the selected area electron diffraction (SAED) pattern as shown in Fig. 10C showcases prominent concentric rings with bright spots as the characteristics of a polycrystalline structure. The diffraction rings correspond to various crystallographic planes of silicon, further confirms the crystallinity retention after treatment. The observed diffraction rings were analysed to determine the corresponding interplanar spacings (d-spacing values) in Fig. 10D. The prominent diffraction rings are indexed to the characteristic planes of silicon like (111), (220), (311) and (400) respectively.

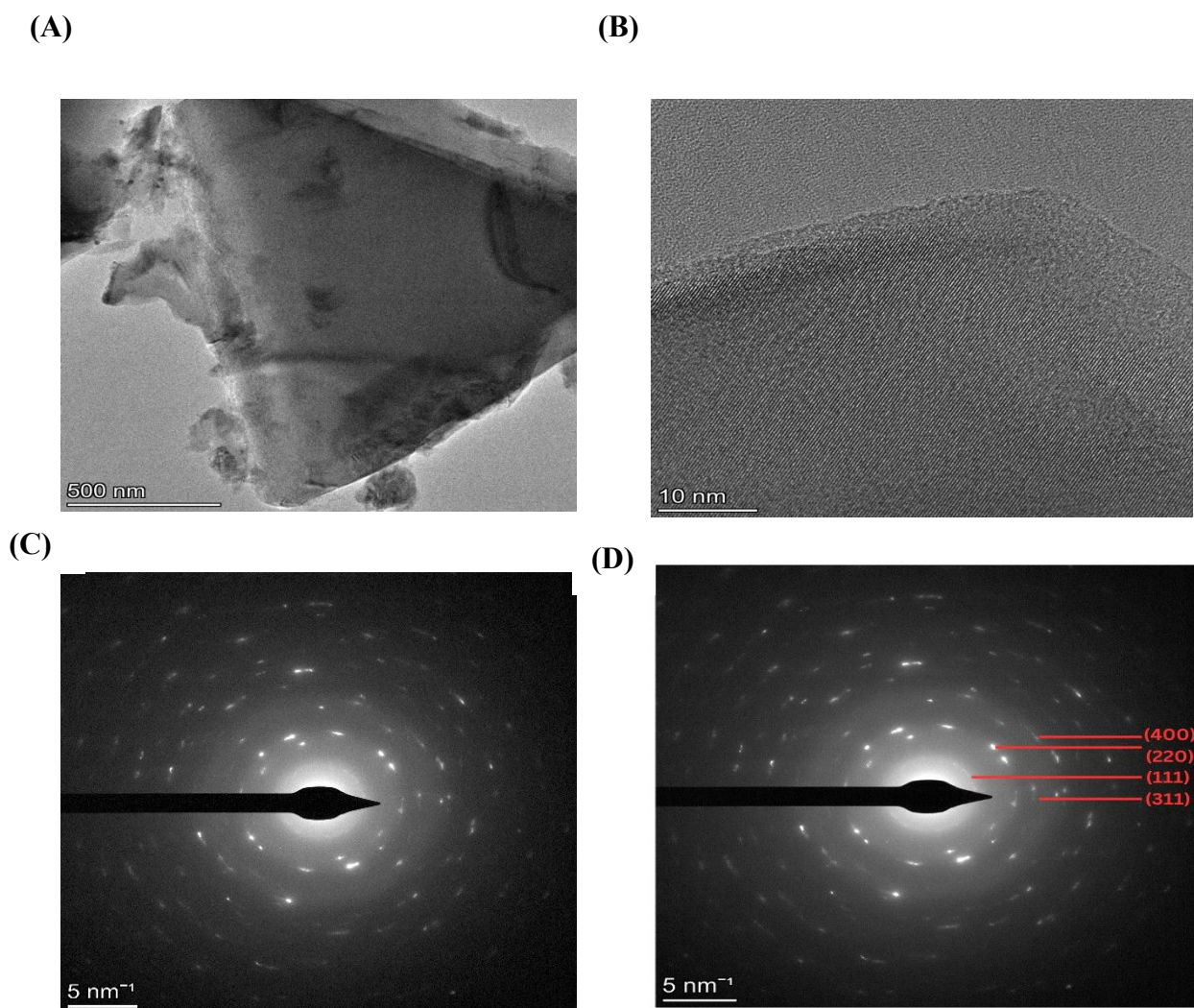


Fig. 10 Transmission electron microscopy image of the prepared recycled silicon powder after chemical treatment: (A) Bright field TEM image highlighting agglomerated and irregularly shaped silicon particles having dimensions in the sub-micron range. The (B) shows the high-resolution TEM image revealing the presence of noticeable lattice fringes that confirms the crystalline nature of the silicon, (C) selected area electron diffraction (SAED) pattern exhibiting the presence of diffraction rings with bright spots, indicative of a polycrystalline structure. The



D) represents the indexed SAED pattern where the diffraction rings are assigned to the (111), (220), (311), and (400) crystallographic planes of crystalline silicon, based on the analysis of calculated d-spacing.

### 3.6. X-ray Fluorescence Spectroscopy analysis

The quantitative analysis of the recovered silicon powder was carried out through the Wavelength Dispersive X-ray Fluorescence Spectrometer (WD-XRF; ElvaX spectrometer) having Helium target to check the purity of the sample. This quantitative analysis of the sample as characterized through XRF is shown in Fig. S2A. The X-ray Fluorescence spectrum shows a major Silicon peak with maximum intensity and having a concentration of 99.52%. Along with silicon, other elemental impurities like Fe, Ca, Cr, V, Ti, S, Mn are detected respectively. Extremely low concentrations of Cu, Ag and other remaining elements implies that these impurities have negligible impact on the purity of the material.<sup>36</sup> The Fig. S2B highlights the X-ray Fluorescence intensity spectrum in which Si -  $K_{\alpha}$  has the majority peak. Furthermore, the other peaks of Fe, Ca and Ag have comparatively very smaller intensity and the absence of any other additional strong peaks confirmed that no other major phases are present in the recovered silicon powder. Hence, the XRF results indicates that the recovery process produces silicon ( purity 99.52 %) with minimal impurities. The observed purity describes about the efficient recovery of silicon from waste solar panels and ensuring the suitability of the material for preparation of the electrodes.

### 3.7. BET surface area analysis

The BET (Brunauer–Emmett–Teller) analysis of the recycled silicon powder after chemical treatment was performed to calculate the pore structure and the surface properties of the powder. The analysis is based on both the desorption and adsorption plots. The desorption plot shows a gradual increase in the cumulative pore volume with increasing pore diameter, whereas the pore size distribution  $dV(d)$  exhibits a higher contribution from smaller pores, indicating the formation of a mesoporous structure. Similarly, in case of the adsorption plot the cumulative pore volume increases progressively with increasing pore diameter along with the significant presence of smaller pores. The close agreement between the desorption and adsorption curves shows the formation of a mesoporous structure in the chemically treated recycled silicon powder.

The nitrogen desorption and adsorption isotherm of the chemically treated recycled silicon powder as shown in Fig. 11C illustrates a gradual increase in adsorbed volume with increasing



relative pressure ( $P/P_0$ ) that reflects a continuous pore filling process across the complete relative pressure range. The adsorption and desorption curves form a hysteresis loop, which is the characteristic of mesoporous structures associated with condensation within narrow pores.

At low relative pressure values, the gradual enhancement in adsorption indicates about the low content of micro-pores as well as the initial surface adsorption, whereas the increased adsorption at higher relative pressures shows about the multilayer adsorption within mesoporous structures. The isotherm describes the Type – IV plot, that shows the characteristics of mesoporous materials by confirming the development of porous structure after chemical treatment. The small separation between adsorption and desorption curves shows appreciable pore connectivity and also favourable for ion transport. The surface area of the powder sample from the BET analysis is found to be  $1.544 \text{ m}^2/\text{g}$ .

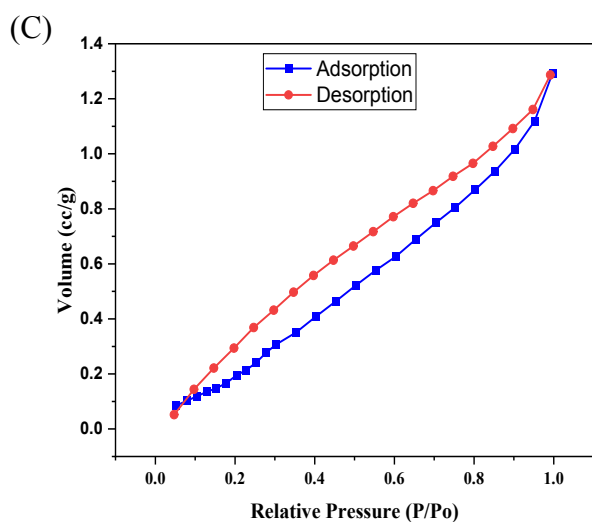
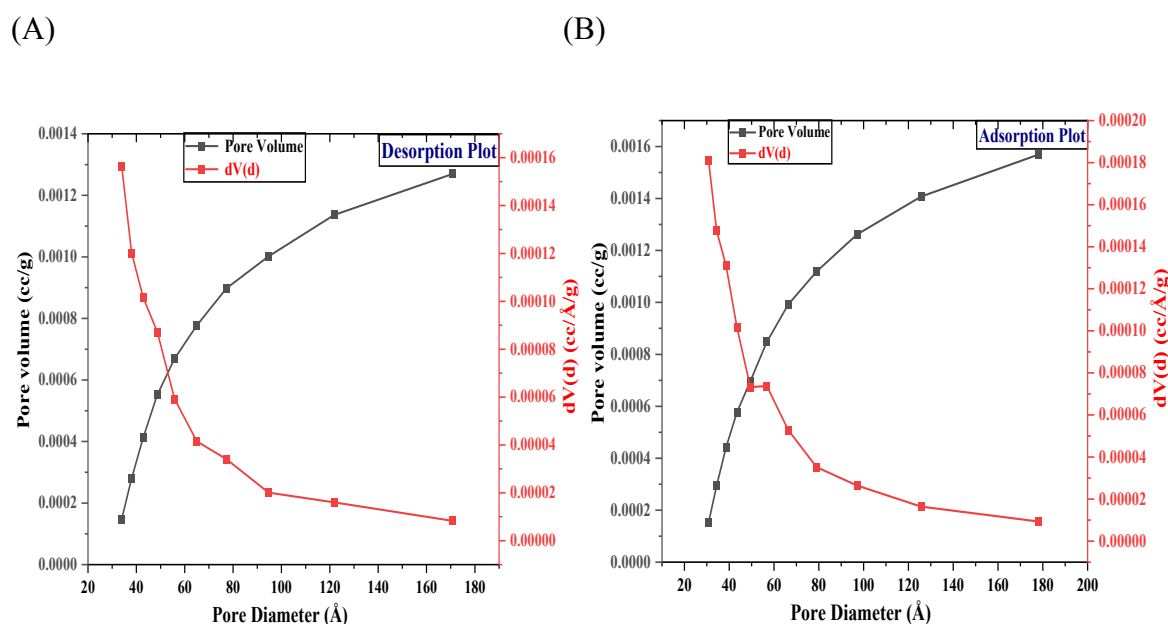


Fig. 11 (A) BET desorption results of the recycled silicon powder after chemical treatment highlighting the variation of cumulative pore volume and pore size distribution with pore diameter. This plot describes the increase in pore volume along with a larger contribution from smaller pores by suggesting the formation of moderate mesoporous structure. Fig. 11 (B) BET pore structure analysis from the adsorption plot of the recycled silicon powder prepared after chemical treatment. This plot is showing the increase in cumulative pore volume with pore diameter, whereas the pore size distribution curve reveals a higher density of smaller pores, that also confirms the presence of a porous structure after chemical treatment. Fig. 11(C) Nitrogen adsorption-desorption isotherm of the chemically treated recycled silicon powder measured from BET data analysis. The volume of nitrogen adsorbed (cc/g) is plotted against relative pressure ( $P/P_0$ ), which is showing a continuous increase in adsorption along with the increase in relative pressure. The occurrence of a small hysteresis between the adsorption and desorption curves indicates the presence of mesoporosity. The observed shape of this isotherm exhibits the characteristics of Type -IV behaviour, describing the formation of mesoporous structure after the chemical treatment.

### 3.8. Thermogravimetric and differential scanning calorimetry analysis

The TGA-DSC analysis of the recycled silicon powder exhibits negligible variation in weight throughout the temperature range up to 800 °C. The nearly constant TGA curve which is  $\approx$  100 % , highlights minimal weight loss that represents high thermal stability and negligible volatile content. A very small reduction in initial weight observed at temperature below 200 °C can be attributed to the removal of residual solvents trapped within the structure of the recycled silicon powder. A slight increase in weight at higher temperatures  $\approx$  200 °C – 600 °C is more likely due to the gradual surface oxidation of silicon under trace oxygen conditions. The DSC curve illustrates a weak endothermic feature in the initial temperature region which is again due to the desorption of moisture or relaxation of surface bound species. A distinct exothermic peak is observed, which is associated with the structural rearrangement within the silicon matrix.



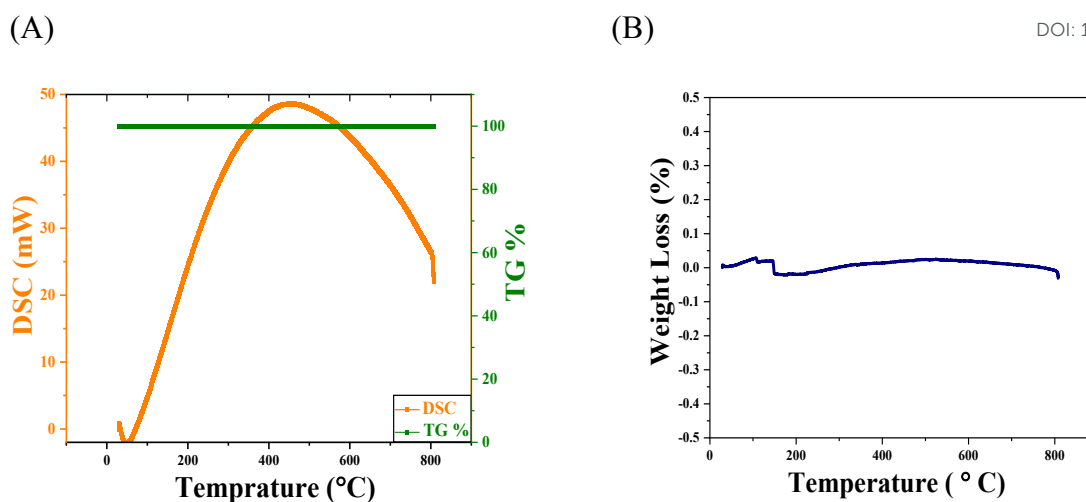


Fig.12 (A) Thermogravimetric analysis (TGA) and Differential Scanning Calorimetry (DSC) plots of chemically treated recycled silicon powder recorded up to 800 °C. The TG % curve showing negligible weight loss ( $\square$  0.03 %), indicating high thermal stability and effective removal of volatile impurities after chemical treatment. The presence of broad endothermic DSC curve highlighting the absence of significant thermal degradation as well as any exothermic reactions. Fig. 12 (B) Thermogravimetric analysis (TGA) curve of the prepared recycled silicon powder after chemical treatment showing negligible variation in weight loss percentage ( $\square$   $\pm$  0.04 %) within the temperature range up to 800 °C, which indicates high thermal stability and minimal presence of the heat – sensitive substances. A minimal change in weight ( $\square$  0.02 % – 0.03 %) below the temperature 200 °C is because of the evaporation of adsorbed moisture along with the loosely bound surface species followed by a nearly stable region with a slight increase in weight between the temperature range from 200 °C – 600 °C. The weight remains constant with slight fluctuations at higher temperature which confirms the absence of significant thermal decomposition.

## Characterizations of the fabricated electrodes

### 4.1. X-ray diffraction Spectroscopy

The Fig. 13A illustrates the X-ray diffraction plot of the electrode made over copper foil, obtained within the range from 10° to 90° on a 2 $\theta$  scale. The most intense diffraction peak was observed at 2 $\theta$   $\approx$  47.18°, which corresponds to the (220) plane of crystalline silicon. This indicates about the highly ordered crystal arrangement of silicon preferably oriented along that direction. Other diffraction peaks located at 28.5°, 56.14°, 69.14°, 76.32° and 87.94° were assigned to the (111), (220), (400), (331) and (422) planes respectively, which further confirms the presence of crystalline silicon. This show that the silicon as active material plays the key



role in the electrode. Apart from these diffracted peaks of silicon other two peaks observed at around  $2\theta \approx 43.22^\circ$  and  $2\theta \approx 50.26^\circ$  represents the (111) plane and (200) plane of the crystalline copper substrate which is present below the electrode film. A polymer Polyvinylidene Fluoride (PVDF) was used as binder during the preparation of the electrode to increase adhesion of active material with the substrate and therefore a minor peak at around  $2\theta \approx 20.0^\circ$  is obtained which corresponds to the (110) plane of the crystalline  $\alpha$ -phase of PVDF. In addition to that a small diffraction peak was observed around  $2\theta \approx 30.30^\circ$  which relates to the (102) plane of silicon dioxide ( $\text{SiO}_2$ ). This peak reveal that a small amount of silicon was partially oxidized at the surface.

The X-ray diffraction plot of the electrode prepared of recycled silicon as active material over the graphite sheet, observed within the range from  $10^\circ$  to  $90^\circ$  on a  $2\theta$  scale is shown in the Fig. 13B. The most intense diffraction peak was observed at  $2\theta \approx 47.36^\circ$ , which corresponds to the (220) plane of crystalline silicon. The other diffraction peaks observed at  $28.54^\circ$ ,  $56.18^\circ$ ,  $69.18^\circ$ ,  $76.4^\circ$  and  $88.08^\circ$  were assigned to the (111), (220), (311), (400), (331) and (422) planes respectively. Further, these planes confirm the presence of crystalline silicon. Other than the presence of active material silicon, a diffraction peak at  $30.3^\circ$  corresponds to the (102) plane of silicon dioxide. Furthermore, the presence of two peaks observed at around  $2\theta \approx 26.38^\circ$  and  $2\theta \approx 54.58^\circ$  indicates about the (002) and (004) plane of the substrate graphite sheet. The XRD pattern also contains a very small peak at around  $2\theta \approx 20.0^\circ$  similar as that of Cu foil substrate which describes about the (110) plane of crystalline PVDF.<sup>37</sup>



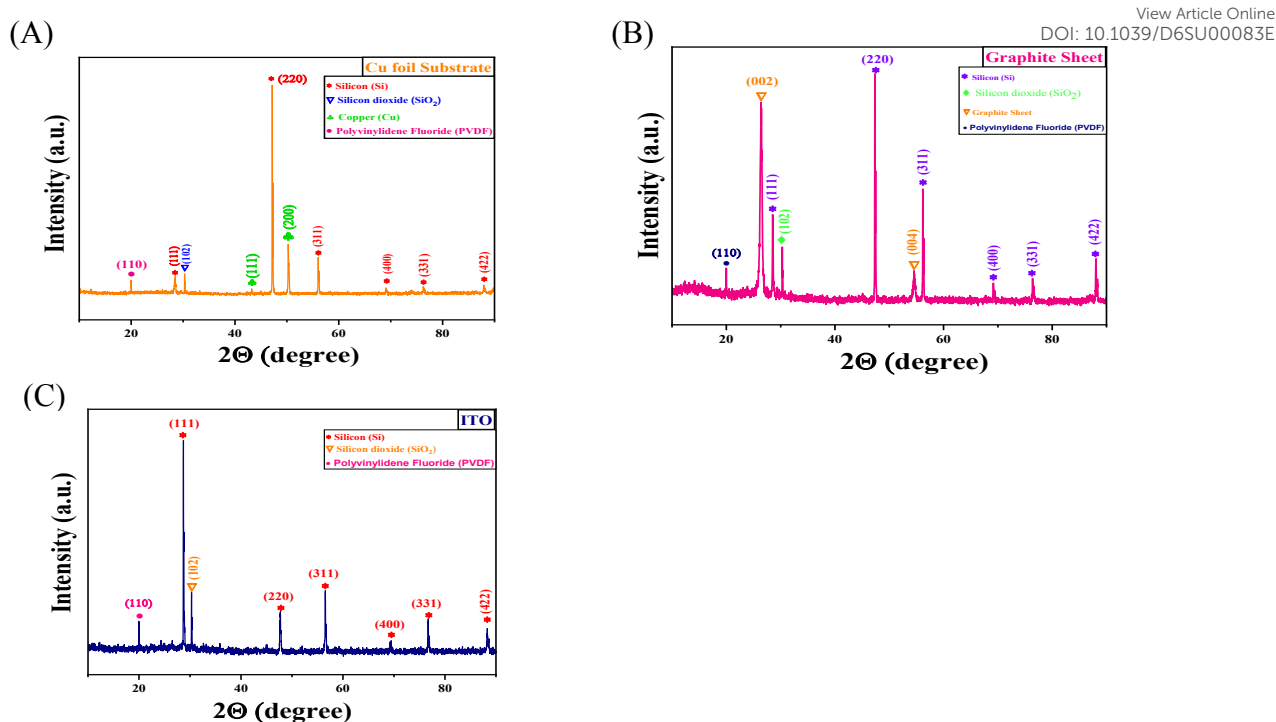


Fig.13 XRD plots of the Si/SiO<sub>2</sub> composite electrode fabricated over different substrates (A) Copper foil, (B) Graphite Sheet, (C) ITO Substrate. The presence of the diffraction peaks corresponding to the planes (111), (220), (311), (400), (331) of the crystalline silicon are observed in case of all the three substrates. The existence of SiO<sub>2</sub> indicates partial oxidation of the material. In addition to this in (A) distinct peaks of the copper substrate are present, whereas in (B) a strong peak  $\square 26^\circ$  corresponds to the (002) plane of the graphite, but in case of ITO no such peaks of substrate are observed. The existence of the binder is also observed in case of all the substrates.

The Fig. 13C shows the X-ray diffraction plot of the electrode over the ITO substrate, observed within the range from  $2\theta \approx 10^\circ$  to  $2\theta \approx 90.0^\circ$ . Similar to that of the slurry deposited over other two substrates the XRD peak at  $2\theta \approx 20^\circ$  indicates the (110) plane of crystalline PVDF. In addition, the peak at  $2\theta \approx 30.3^\circ$  highlights the presence of (102) plane of SiO<sub>2</sub>. The most intense peak was observed at  $2\theta \approx 28.72^\circ$ , which indicates the (111) plane of crystalline silicon. The maximum intense peak corresponds to (111) plane is differed from that of the most intense peak of Si in case of the other two substrates might be because of the factors like deposited film thickness, difference in preferred crystallographic orientation or due to the substrate diffraction. The other diffraction peaks observed at  $47.68^\circ$ ,  $56.54^\circ$ ,  $69.46^\circ$ ,  $76.72^\circ$  and  $88.3^\circ$  corresponds to (220), (311), (400), (331) and (422) planes of crystalline silicon respectively.



## 4.2. SEM- EDAX analysis

View Article Online  
DOI: 10.1039/D6SU00083E

The micro - structural analysis of the composite electrodes prepared by depositing over copper foil, ITO and graphite sheet were characterized using field emission scanning electron microscopy (FESEM). The FESEM micrograph obtained for the electrodes made over copper foil in Fig. 14A exhibit a rough and non- homogeneous surface identified by randomly distributed particles with flake – like segments. This composite electrode morphology consists of closely packed irregular grains along with fine particles forming a compact network arrangement. The tightly packed configuration minimizes void formation by strengthening the intimate conductive pathway or charge transport network across the Si/SiO<sub>2</sub> and conductive carbon nanotubes network. Fig. 14B confirms the elemental composition of the coated slurry. The major Silicon peak as shown in the Fig. S3A with 62.00 wt.% and 78.74 atomic % highlights that the silicon constitutes the primary portion of the electrode and the prepared electrode surface is mainly Si- rich. The second major component present in the electrode slurry is carbon with a weight percentage of 28.77% and atomic percentage of 15.62%, which mainly comes from the CNTs. A minor peak of Fe with 4.64 wt.% and 1.27 atomic % signifies the presence of residual iron (Fe) catalyst particles originating from the carbon nanotubes synthesis process as iron often employed as catalyst during CNT functionalization.

The FESEM image of the silicon composite slurry coated ITO substrate is shown in the Fig. 14C. The surface morphology of this electrode highlights larger and angular domains having sharp edges along with intense contrast, which corresponds to the crushed silicon pieces from recycled silicon solar cells. As shown in the Fig.14C, the silicon particles appear densely packed in some regions, whereas in some other regions these particles are surrounded by uniformly distributed fine particles originate from the surface oxidation of silicon. The aggregation of smaller particles attached to the silicon grains showing the presence of SiO<sub>2</sub> and thin elongated string-like structures are the CNTs embedded within the silicon grains. The low contrast regions appeared in the image corresponds to the PVDF binder that holds the silicon and CNT firmly over the ITO substrate. The EDAX data in the Fig. 14D indicates that the major contribution come from silicon which is approximately around 55.53 wt.% and 74.15 at.%. A considerable amount of carbon (approximately around 35.23 wt.%) is present which is because of the CNTs added as conductive additive. A small content of oxygen (□ 4.10 wt.%) and Fe (□ 4.66 wt.%) show the presence of surface oxide and traces of Fe used as catalyst during the synthesis of CNTs. A negligible amount of aluminium (□ 0.48 wt.%) is also observed. The EDAX spectrum shown in Fig. S3B describes a sharp peak corresponding to



silicon, ensuring that the main component in the recovered powder is silicon. In addition to this, minor peaks correspond to C, Fe, O and a very small peak corresponding to Al is also present which indicate the presence of surface impurities.<sup>38</sup>

From the FESEM image in Fig. 14E the surface morphology of the slurry coated graphite sheet substrate, show that the deposited slurry forms a surface mainly composed of large, angular crystalline silicon particles originated from the crushed silicon wafers. These larger crystalline silicon flakes were surrounded by smaller, fine and irregular particles, which correspond to surface SiO<sub>2</sub> formed because of the chemical treatment. The regions having low contrast highlights the presence of PVDF, which acts as a binder that occupies the voids and holds the silicon and SiO<sub>2</sub> particles firmly over the graphite substrate. This can facilitate the diffusion of electrolyte during electrochemical cycling process. The energy dispersive X-ray spectrum and elemental composition of this electrode is shown in Fig. S3C and Fig. 14F. The dominant silicon peak corresponds to nearly around 95.55 wt.% and 94.77 atomic % along with very small content of oxygen arising from surface oxide. A very small peak of Fe with 2.02 wt.% and 1.01 atomic % indicates the presence of residual iron catalyst particles associated with CNT synthesis process.

Thus, the collective FESEM – EDAX results show that the electrode slurry is mainly composed of silicon with a minor oxide content and is uniformly integrated within the CNT-PVDF network over the graphite sheet substrate.



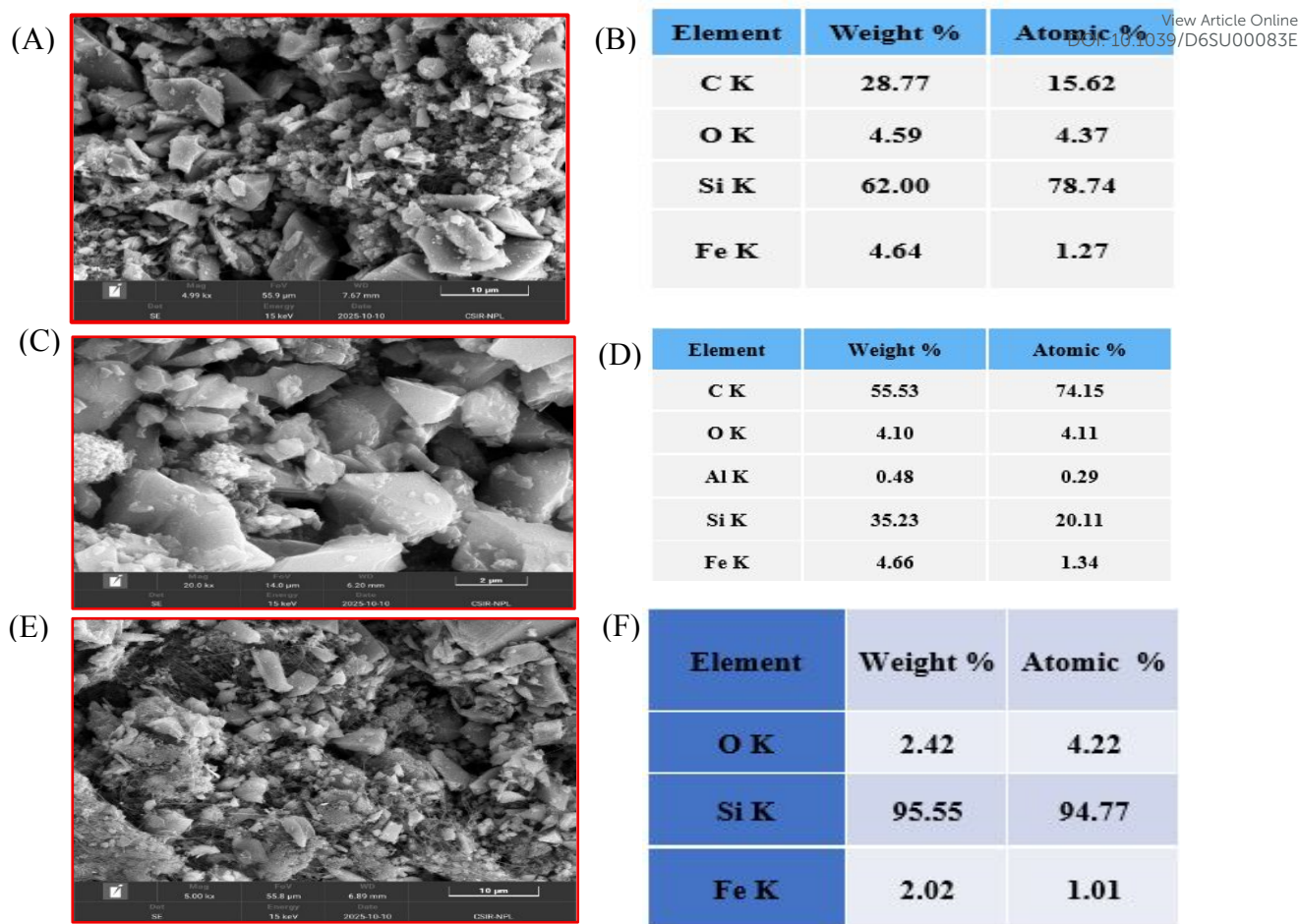


Fig. 14 (A) FESEM image of the silicon-based composite electrode prepared over Cu foil, showing aggregated particles with heterogeneous morphology and non-uniform spatial distribution with its (B) corresponding EDAX analysis displaying Si as the major wt.% element along with the contributions from C, O and minor traces of Fe. (C) FESEM image of the slurry coated ITO substrate electrode showing comparatively more uniform and compact particle arrangement and its (D) corresponding EDAX data indicating increase in the content of carbon as conductive additives. (E) FESEM image of the electrode made over graphite sheet showing uniformly distributed particles with reduced agglomeration and improved surface uniformity with its (F) corresponding EDAX results confirming the presence of a larger content of Si along with decrement in oxygen and impurity wt.%

### 4.3. Raman Spectroscopy analysis

The Raman spectroscopy plot of the silicon composite slurry deposited copper foil is shown in the Fig. 15A. This plot describes about the distinct vibrational bands corresponding to the different structural constituents of the electrode. The strongest peak occurs at  $514.72 \text{ cm}^{-1}$ , which indicates the first-order optical phonon mode of crystalline silicon. The high intensity



of this peak signifies that the recycled silicon mainly conserves its crystalline nature even after the deposition of the slurry over the substrate. A weak band observed at  $\square$   $301.26 \text{ cm}^{-1}$  might be because of the higher order phonon scattering process resulting from the surface defects. A broad band observed nearly around  $951.77 \text{ cm}^{-1}$  highlights the presence of Si-O-Si or Si-OH vibrations which was occurred because of the formation native oxide layer over surface of silicon. This also shows that silicon is the key Raman active material although the presence of  $\text{SiO}_2$  is there. Other than the active material related modes, a peak at around  $1595 \text{ cm}^{-1}$  highlights the presence of G-band of carbon originate from the carbon nanotubes added as a conductive additive to the slurry.

The Fig. 15B shows the Raman spectra of the electrode prepared by depositing silicon composite slurry over the ITO substrate. Among the different vibrational bands, the highest and intense peak is observed at  $\square$   $510 \text{ cm}^{-1}$ , which corresponds to the characteristics of the primary optical phonon vibrations of crystalline silicon. This downshift behaviour from that of the bulk silicon is because of the strain within the silicon particles. The weaker intensity band observed at  $\square$   $294.95 \text{ cm}^{-1}$  signifies the secondary and defect linked silicon vibrations, which is the reason of heterogeneous silicon domains. A small and broad peak detected at  $\square$   $940.78 \text{ cm}^{-1}$  indicates the Si-O-Si stretching band which is formed during the recycling process.

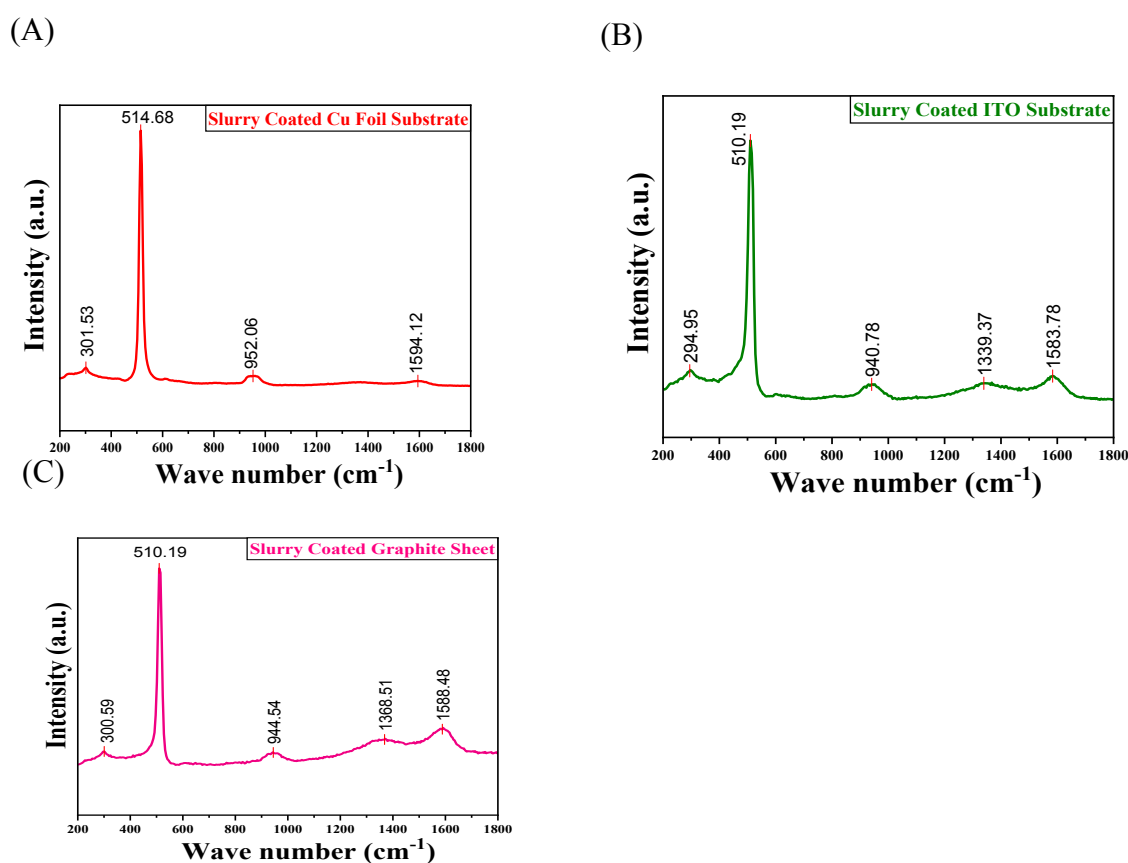


Fig. 15 Raman spectroscopy plot of slurry deposited electrodes over (A) Cu foil, (B) ITO and (C) Graphite sheet. In all the three plots, the characteristic vibrational bands of the active material silicon are observed. The spectrum recorded for (A) Cu foil exhibits a prominent peak with reduced background intensities, indicating good coating over the substrate. (B) For ITO additional low-intensity bands are found because of the conductive oxide layer and for (C) graphite sheet the spectrum displays broader peaks along with the increased background intensity due to the graphite substrate and its interaction with the coated layer.

The two broad peaks featured at  $\square 1339.37 \text{ cm}^{-1}$  and  $\square 1583.78 \text{ cm}^{-1}$  represent the D-band and G-band of carbon, describing the co-existence of both defects linked disorder-ness and ordered nature due to  $\text{sp}^2$  network, which is the characteristics of CNTs.<sup>39</sup> The Raman vibrational spectrum of the slurry deposited over the graphite sheet shows different characteristic vibrational modes related to silicon, silicon oxide and carbon – based components as shown in Fig. 15C. The most dominant peak is appeared at  $\square 510.19 \text{ cm}^{-1}$ , which is due to the fundamental optical phonon vibration associated with crystalline silicon. The shift of this peak signifies about the occurrence of lattice strain and phonon confinement inside the lattice. Although the downshift in the peak occurred, but the intensity showcases the presence of crystalline nature of silicon in the heterogeneous mixture. In this case, also a weaker peak is observed at  $\square 300.58 \text{ cm}^{-1}$  which is linked to defect - activated secondary silicon vibrations. Again, a moderate intensity peak nearly around  $\square 945 \text{ cm}^{-1}$  represents the stretching vibrations between silicon and oxygen, which validates the existence of oxide within the composite material. The two broad bands shown in the figure at  $\sim 1369 \text{ cm}^{-1}$  and  $\square 1588 \text{ cm}^{-1}$  corresponds to the D – band and the G- band of carbon, which highlights the characteristics of disordered and ordered domains of carbon nanotubes.

#### 4.4. Cyclic Voltammetry results analysis

The Fig. 16D highlights the cyclic voltammetry (CV) curves of the electrodes prepared over the copper foil, analysed at different scan rates of 25 mV/s, 50 mV/s, 75 mV/s and 100 mV/s within the potential range from -0.6 V to +0.6 V. The CV curve analysed at the scan rate of 25 mV/s exhibits a nearly symmetric loop with well-defined anodic and cathodic peaks at +0.1786 V and -0.1582 V respectively. The cathodic peak corresponds to the lithiation process of silicon and the formation of  $\text{Li}_x\text{Si}$  phases. During the anodic potential sweep the broad anodic peak is observed at +0.178 V, which describes the de-lithiation process of  $\text{Li}_x\text{Si}$  with the partial reformation of silicon. The nearly symmetric cathodic and anodic behaviour along with the



potential difference of  $\sim 0.336$  V shows very negligible polarization and appreciable electrochemical reversibility which confirms effective charge transport and lithium-ion diffusion across the surface of the electrode. The conductive CNT network enhances the electron movement during electrochemical cycling, whereas silicon and silicon oxide domains help in  $\text{Li}^+$  insertion and extraction. At a scan rate of 50 mV/s, the cathodic and anodic peaks remain distinguishable with a slight shift towards -0.23 V and +0.32 V respectively. This shift indicates a minimal increase in polarization and diffusion resistance, which occurs from lesser time than that of 25mV/s available for the  $\text{Li}^+$  transport at higher scan rates. The presence of well-defined peaks confirms that the lithiation and de-lithiation process remain reasonably reversible which signifies appreciable electrochemical performance and suitability for battery type energy storage applications. The incomplete loop is primarily due to the higher polarization, which describes that electrochemical response of the prepared electrode is sensitive to the scan rate and an ideal rate of potential change is required to maintain balance between diffusion of lithium ions and decrement of side reactions. With the increase in the scan rate up to 75 mV/s, the cyclic voltammetry curve signifies a nearly symmetric, but broader curves explaining co-existence of both faradaic and capacitive type charge storage behaviour. In this curve the cathodic peak is observed near -0.36 V, which indicates lithiation of silicon and the  $\text{Li}_x\text{Si}$  alloy formation. The weak anodic peak in this curve describes incomplete de-lithiation because of slow diffusion of  $\text{Li}^+$  ions across the silicon-electrolyte interface or the presence of residual SEI (Solid-Electrolyte Interface) layer formed in the lithiation process.<sup>40,41</sup> At a higher scan rate of 100 mV/s, the cyclic voltammetry curves show broad and less distinct anodic peaks with an increased gap in the potential between the peaks. The cathodic peak is detected at -0.376 V, whereas the anodic peak is flat and weak that indicates a rise in polarization and slower charge transfer behaviour. The reduced anodic current density at this higher scan rate is due to the incomplete de-lithiation of  $\text{Li}_x\text{Si}$  phases along with increased charge transfer resistance and high capacitive effects that suppress the contribution from faradaic process.

The cyclic voltammetry curves of the electrodes made from a slurry containing recycled silicon as active material deposited over ITO substrates, observed at various scan rates of 25 mV/s, 50 mV/s, 75mV/s and 100 mV/s within the applied potential range from -0.5 V to +1.5 V is shown in the Fig. 16E. At the scan rate of 25 mV/s, the CV curves show smallest currents and narrowest area under the curve. In comparison to higher scan rates, the forward and reverse cycles are very close in this scan rate which indicates that the slower scan rate



allow more complete surface redox reactions and reduced polarization. The broad cathodic and anodic peaks at this scan rate represents the near-equilibrium state where both the diffusion-controlled reactions and slower faradaic reaction process contribute significantly to the current density response. When the scan rate is increased to 50 mV/s, the applied potential range becomes wider and the maximum current density value increases to +0.16 mAcm<sup>-2</sup>. The Cyclic voltammetry curve spreads out more which suggests about the improved capacitive behaviour with the increase in the scan rate. The maximum anodic current density occurs nearly around 1.4 V, whereas the cathodic peak current density occurs at around -0.5 V which indicates steady and stable electrochemical behaviour of the electrode. . At the scan rate of 75 mV/s, the magnitude of current density increases to the maximum value + 0.20 mAcm<sup>-2</sup> with the CV curve spreading outward prominently. The broadest CV loop is observed at the highest scan rate of 100 mV/s with the maximum anodic current density value □ + 0.23 mAcm<sup>-2</sup> and the cathodic current density value □ - 0.21 mAcm<sup>-2</sup>. The preservation of the quasi – rectangular shape of the curve at this comparatively higher scan rate indicates efficient charge – discharge capability and negligible polarization.

The CV curves obtained for the silicon composite slurry deposited electrode over the graphite sheet substrate at different scan rates ranging from 25 mV/s to 100 mV/s within the potential range from – 0.8 V to 1.4 V is shown in the Fig. 16F. At 25 mV/s the curve displays a symmetric loop with smooth variations of current throughout the potential window. The charge storage is mainly controlled by the surface regulated capacitive process and the current variation becomes limited at this rate, suggesting slower ion transport near the electrode - electrolyte interface. At the scan rate of 50 mV/s, the magnitude of the current increases and results a more broader loop. Though the loop becomes broad with increased scan rate, but the shape of the loop remain preserved indicating stable interfacial charge - transfer behaviour. When the scan rate is increased to 75 mV/s, the loop further expands along with the increase in current density upto 1.45 mAcm<sup>-2</sup> and the increase in it along with the increase in scan rate supports the electrical double layer formation rather than bulk insertion process. At the highest scan rate of 100 mV/s, the curve shows the spread with current density ranging from -0.52 mAcm<sup>-2</sup> to 0.68 mAcm<sup>-2</sup>. The CV curve becomes more elongated due to the increased polarization effects along with the accelerated ion shifting at the interface of the electrode.

The cyclic voltammetry (CV) curves of the silicon composite slurry-coated copper foil electrode measured at a scan rate of 5 mV/s and 10 mV/s shows a non-rectangular shape with broad cathodic and anodic features, highlighting the charge storage mechanism involving both



faradaic reactions combined with capacitive behaviours in Fig. 16A. Lithium ions are inserted into the silicon framework to form  $\text{Li}_x\text{Si}$  phases during the cathodic scan, whereas during the anodic sweep the de-lithiation process occurred within +0.3V to +0.5V that confirmed the reversibility of electrochemical process. The broad nature of redox peaks reveals the composite structure of the material along with its partial amorphous nature due to the formation of silicon oxide during chemical treatment. The increase in the current response with the increasing scan rate is clearly observed from the curves but the complete retention of the shape of the curve suggested about the electrochemical stability and reversibility.

The CV plots of the silicon composite slurry deposited over ITO substrate as shown in Fig. 16B displays a non-rectangular shaped curve, indicating a combination of electric double layer capacitance behaviour along with the faradaic redox processes. The presence of broad cathodic and anodic peaks represents the distribution of surface-driven electrochemical reactions across various active sites within the composite material. A noticeable rise in current is observed with the increase in the scan rate from 5 mV/s to 10 mV/s because of the limitations in diffusion process along with the increment in the effects due to polarization.

The Fig. 16C shows the cyclic voltammetry curves of the silicon composite slurry deposited over graphite sheet. At a scan rate of 5 mV/s, the shape of the curve is non-rectangular along with broad cathodic and anodic features that indicates the involvement of both surface capacitive effects as well as faradaic reactions. The lower scan rate allows enough time for the ions of the electrolyte to penetrate into the structure of the electrode, leading to the better use of active sites along with a more accurate electrochemical behaviour. When the scan rate is increased to 10 mV/s, an increment in the current density is observed along with the expansion of the CV loop. At this higher scan rate, ion diffusion into the inner regions of the electrode becomes restricted, and the electrochemical process is increasingly governed by surface-controlled reactions. In addition to that, a minor shift in the oxidation and reduction peak is because of the polarization effects and internal resistance within the electrode system.



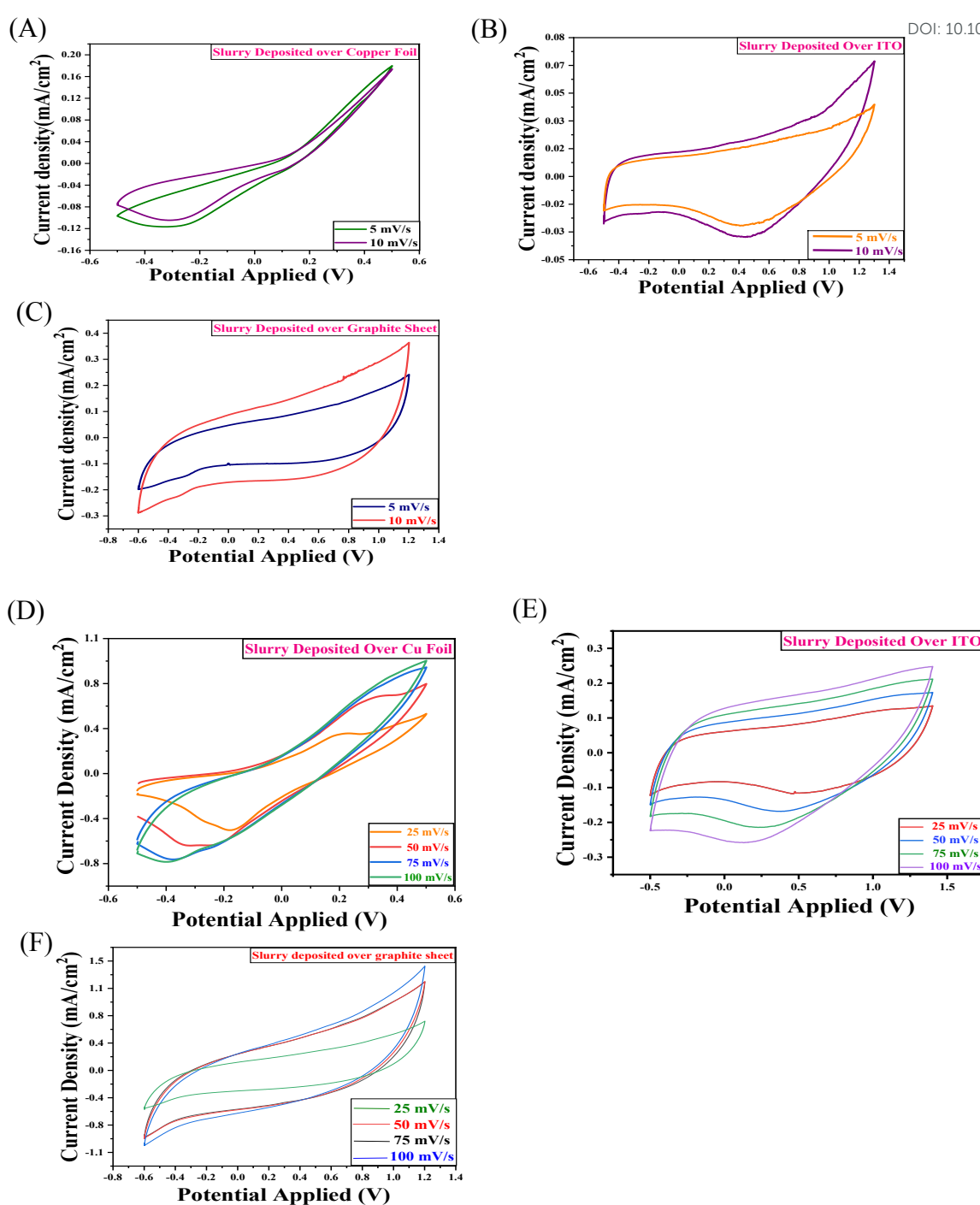


Fig. 16. CV curves of slurry coated electrode over three different substrates (A) Cu foil (B) ITO and (C) graphite sheet measured at the scan rates 5 mVs<sup>-1</sup> and 10 mVs<sup>-1</sup>. The plot in (A) shows a quasi-rectangular shape suggesting the co-existence of faradaic process and the double layer capacitance over the Cu foil electrode. In (B) the curves display increased current response along with redox behavior, indicating improved electrochemical activity due to the ITO substrate and the CV curves in (C) showing wider loop areas and appreciable shapes reflects better charge storage behavior as well as effective interaction between the active material and the graphite sheet substrate. Fig. 16. CV curves of slurry coated electrode over



three different substrates (D) Cu foil, (E) ITO and (F) graphite sheet obtained at the scan rates ranging from 25  $\text{mVs}^{-1}$  and 100  $\text{mVs}^{-1}$ . The plot in (D) shows well defined cathodic and anodic peaks at the lower scan rates (25  $\text{mVs}^{-1}$  and 50  $\text{mVs}^{-1}$ ) indicating the occurrence of lithiation and de lithiation of silicon along with the shifting and broadening of peaks with increased scan rate. In case of (E) expansion of CV curves with the increment in scan rate is observed and the retention of the actual shape of the curve at higher scan rates indicate efficient electrochemical activity over the ITO. The plots in (F) exhibit nearly symmetric and progressively broader loops with increasing scan rate, which reflects a capacitive process along with an appreciable interfacial charge transfer.

View Article Online  
DOI: 10.1039/D6SU00083E

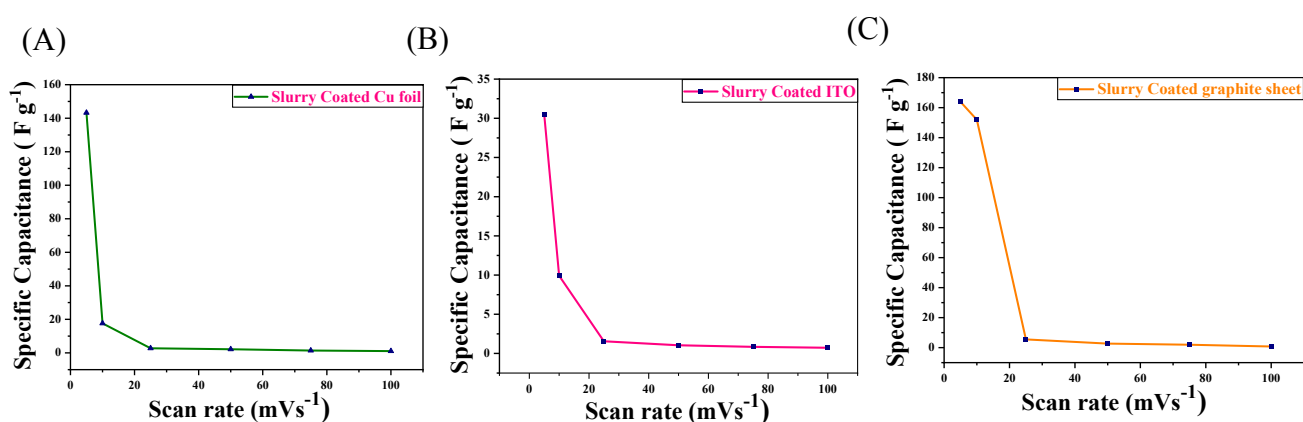


Fig. 17. Scan rate v/s Specific Capacitance plots of (A) slurry coated Cu foil electrode (B) slurry coated ITO substrate and (C) slurry coated graphite sheet electrode with scan rate ranging from 5  $\text{mVs}^{-1}$  up to 100  $\text{mVs}^{-1}$ .

The specific capacitance ( $C_p$ ) values for coated Cu foil, ITO and graphite sheet were calculated from the CV plots at different scan rates. The maximum value of specific capacitance for Cu foil electrode was found to be 143.23  $\text{F g}^{-1}$ , appeared at the scan rate 5  $\text{mV/s}$ . Also, the maximum value of specific capacitance for ITO and graphite sheet was reported to be 30.53  $\text{F g}^{-1}$  and 163.92  $\text{F g}^{-1}$  respectively at the scan rate 5  $\text{mV/s}$ .

#### 4.5. Electrochemical Impedance Spectroscopy results analysis

The Fig. 18A represents the Nyquist plot of the electrode made over copper foil. The impedance curve shows a semicircle in the high- frequency region to medium-frequency region followed by an inclined line in the low-frequency region, implying lithium-ion diffusion behaviour. In the high frequency region, the intercept of the Nyquist plot on the  $Z'$  axis corresponds to the solution resistance  $R_s$  of  $\sim 20 \Omega$ , which mainly occurs due to the resistance of the electrolyte, and the internal interface. In addition to this, the occurrence of a distinct semicircle in the mid-



frequency region indicates a charge-transfer resistance  $R_{ct}$  of  $\sim 290 \Omega$ , which arises because of the limited lithium-ion exchange and charge transfer reactions between the active material and the electrolyte. At low frequencies beyond the semi-circular portion, the Nyquist plot shows a nearly vertical inclination from  $\sim 37.62 \Omega$  to  $\sim 331.42 \Omega$ , which shows the characteristics of Warburg impedance related to the movement of  $\text{Li}^+$  ion in the bulk of the electrode. This region in the plot shows efficient ion transport through the porous silicon network along with the minor diffusion resistance most likely due to the repeated volume change of silicon during lithiation and de-lithiation.<sup>41,42</sup>

The Fig. 18B represents the Nyquist plot of the coated ITO substrate electrode. This impedance curve also consists of a semi-circular loop in the high frequency region to mid-frequency region, followed by a sharply increasing tail in the low-frequency region. In the high frequency region, the intercept of the Nyquist plot on the  $Z'$  axis represents the solution resistance ( $R_s$ ), which is around  $\square 114 \Omega$ . This resistance occurs mainly from the collective effect of electrolyte, surface of the ITO substrate and the electrode-electrolyte interface. Along with this the presence of a relatively flattened semi-circle in the mid-frequency region describes a charge-transfer resistance  $R_{ct} \square 187.12 \Omega$  which is because the electrode-electrolyte interface is regulated by a combination of surface interactions. In the low-frequency region beyond the semi-circular portion, the plot rises sharply upward by forming a Warburg-type inclination related to the ion diffusion through the porous structures. Therefore, the EIS plot shows moderate charge transfer resistance along with the diffusion-controlled charge dynamics within the silicon composite layer over the ITO substrate.

The EIS plot of the silicon composite slurry-coated graphite sheet describes a distinctly different characteristics compared to the other substrates. The Nyquist plot shows almost a linear plot extending from the high-frequency region to low-frequency region with a very small solution resistance value  $R_s$  of  $\sim 10 \Omega$ . The very small size of the semi-circle indicates that the charge-transfer resistance at the graphite sheet and electrolyte interface describes high electrical conductivity of the graphite substrate along with the continuous conductive pathway formed by the silicon composite slurry. At the low-frequency portion, the linear tail confirms that ion-migration process occurs through the porous electrode structure and electrolyte contributes to the overall impedance.

The equivalent circuits shown in Fig. 18D, Fig. 18E and Fig. 18F for the three fitted electrochemical impedance spectra were also shown with their respective fitted plots. The



circuits consist of elements like  $R_1$ , which represents solution resistance,  $R_2$  represents surface resistance,  $R_3$  is the charge transfer resistance,  $C_1$  and  $C_2$  are for double layer capacitance and pseudocapacitive contribution respectively. Also,  $W_{01}$  stands for the finite Warburg element, whereas  $W_1$  and  $W_2$  are the semi – infinite Warburg elements. CPE stands for constant phase element showing non – ideal capacitive behaviour.

The Fig. 18G , Fig. 18H and Fig.18I show the Bode plots for the slurry deposited over Cu foil, ITO and graphite sheet which provides an additional understanding of the frequency dependent impedance characteristics of the electrodes. At lower frequencies, in case of the Cu foil substrate, the impedance is relatively high indicating slower charge-transport processes and significant interfacial resistance. With the increase in frequency, the impedance drops sharply and eventually approaches a low, frequency-independent region, which signifies improved charge accommodation at higher frequencies. The phase-angle curve displays a noticeable peak around the mid-frequency range.

The silicon composite slurry deposited over ITO substrate electrode shows high impedance at low frequencies showing reduced ion mobility and prominent interfacial polarization effects during slowly varying signals. As the frequency increases, the magnitude of the impedance decreases and make transition into a more stable region. The phase-angle plot shows a well-defined peak in the mid-frequency range, describing a distinct relaxation process associated with interfacial charge redistribution and surface-dominated kinetics. The position and shape of this peak represent faster electrochemical characteristics nature than that of the observed peak in the plot of Cu foil substrate.

In case of the graphite sheet, in the low-frequency region the magnitude of the impedance is very low. This nature of the curve suggests faster charge transport within the graphite network. The decrease in impedance with the increase in frequency is more uniform than that of the other substrates. The phase-angle peak appears at much lower impedance values and the Bode plot clearly establish the graphite sheet substrate as the most conductive among the three.

The obtained  $\chi^2$  values from the EIS fitted data are 1.794 for graphite sheet, 2.205 for Cu foil and 8.141 for ITO based electrodes. The relatively low  $\chi^2$  values in case of graphite sheet and ITO substrate-based electrodes indicate a close agreement between the experimental data and fitted data. A slightly higher  $\chi^2$  value in case of ITO based electrodes is because of the possible surface oxidation and non-ideal electrode-electrolyte interactions. In addition to that a

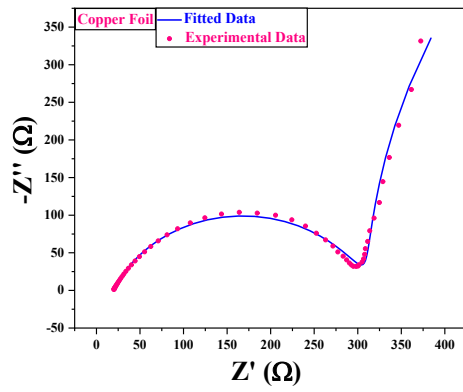


comparison table consisting of  $R_s$ ,  $R_{ct}$  and Warburg parameters for all the three types of electrodes is shown here. View Article Online  
DOI: 10.1039/D6SU00083E

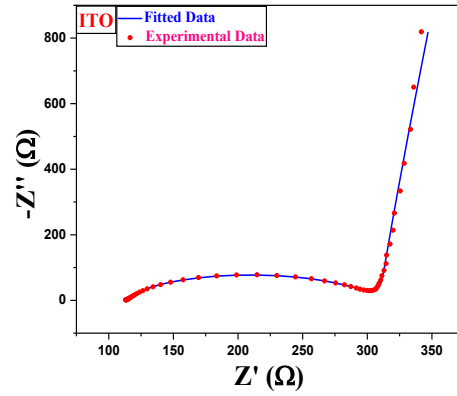
<b>Substrate Type</b>	<b><math>R_s</math> (<math>\Omega</math>)</b>	<b><math>R_{ct}</math> (<math>\Omega</math>)</b>	<b>Warburg</b>	<b><math>\chi^2</math></b>
<b>Graphite Sheet</b>	<b>9.88</b>	<b>16.03</b>	<b><math>A_{w1} = 80.438</math> <math>A_{w2} = 105.08</math></b>	<b>1.794</b>
<b>Copper Foil</b>	<b>19.77</b>	<b>290.55</b>	<b><math>A_{w1} = 2.856</math> <math>W_{or1} = 28.805</math></b>	<b>2.205</b>
<b>ITO</b>	<b>114.11</b>	<b>187.12</b>	<b><math>W_{or1} = 236.64</math> <math>W_{or2} = 0.309</math></b>	<b>8.141</b>



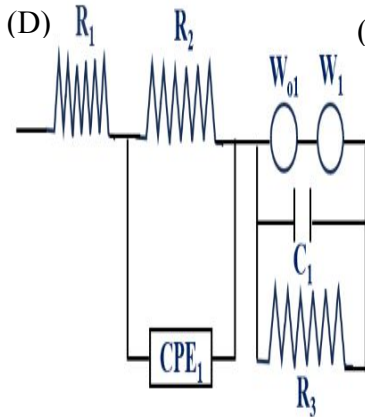
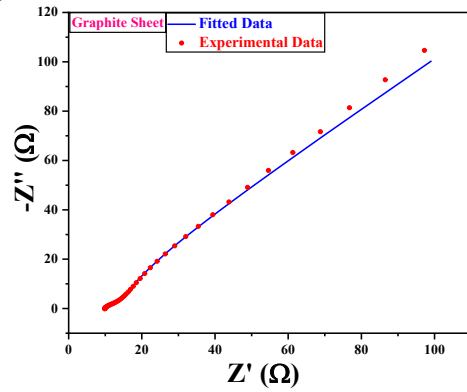
(A)



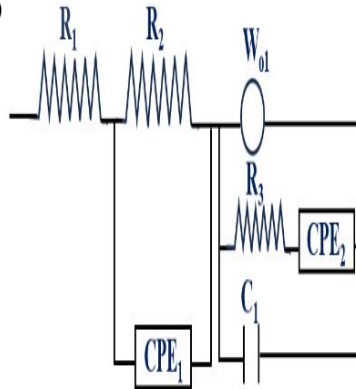
(B)



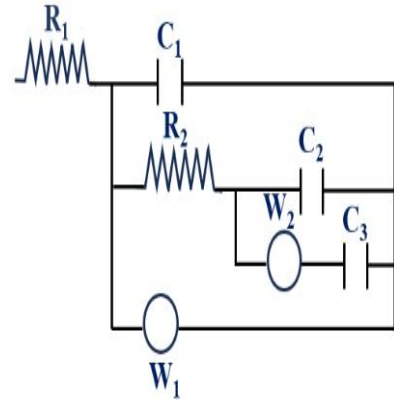
(C)



(E)



(F)



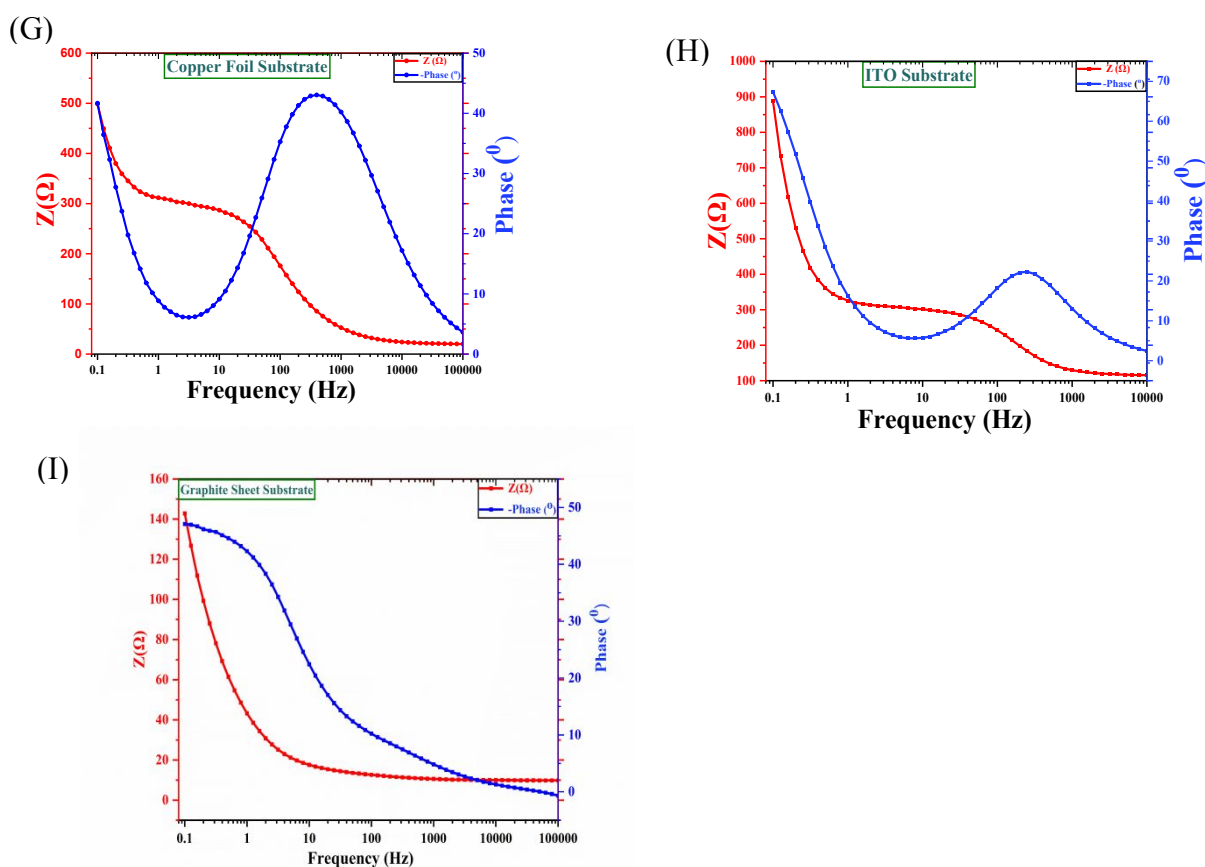


Fig. 18 Electrochemical impedance spectroscopy (EIS) analysis of slurry-coated electrodes: The (A) shows the Nyquist plot of the slurry-coated Cu foil electrode showing experimental data along with the fitted curve, (B) represents the Nyquist plot of the slurry-coated ITO substrate with corresponding fitted data, and (C) illustrates the Nyquist plot of the slurry-coated graphite sheet electrode as well as fitted plot. In (D) of equivalent circuit image is shown, which is used to fit the Cu foil electrode data, (E) shows the equivalent circuit model for the ITO substrate electrode and (F) indicates the equivalent circuit model for the graphite sheet electrode. Fig. 18 Bode plots of slurry-coated electrodes showing impedance magnitude ( $Z$ ) and phase angle ( $^{\circ}$ ) as a function of frequency for (G) slurry-coated Cu foil electrode, (H) slurry-coated ITO substrate, and (I) slurry-coated graphite sheet electrode. In each plot, the red curves represent the impedance magnitude ( $Z$ ), while the blue curves correspond to the phase angle ( $^{\circ}$ ). The value of frequency ranging from 0.1 Hz up to 10 KHz for Cu foil and ITO substrate electrode and 0.1 Hz up to 100 KHz for graphite sheet electrode, illustrating the charge transfer behaviour, interfacial characteristics and frequency-dependent electrochemical response of the respective electrodes.



#### 4.6. Post Cycling X-ray Diffraction Spectroscopy analysis

The post cycling XRD measurements were performed after repeated electrochemical cycling to investigate the structural changes in the electrode material. After 500 GCD cycles, the XRD patterns show some significant changes in the structural characteristics of all the three different types of electrodes. All the diffraction patterns in Fig.19A , Fig.19B and Fig.19C are composed of slightly broadened and less intense crystalline silicon peaks compared to that of the XRD peaks of pre-cycling electrodes, suggesting partial loss of crystallinity along with the occurrence of structural disorder due to the repeated lithiation and de-lithiation cycles. Meanwhile, in case of Cu foil electrode the sharp and intense peaks of the copper substrate confirm its structural stability during cycling. Similarly in case of graphite sheet electrode the most prominent peak at  $\approx 26.8^\circ$  and a minor peak at  $54.9^\circ$  corresponds to the (002) plane and (004) planes of the graphite substrate. The XRD plot of the ITO based electrode highlights the presence of a peak due to the ITO substrate at  $\approx 52^\circ$  that corresponds to its (440) plane. Furthermore, the presence of a broad hump  $\approx 26.5^\circ$  only in the case of Cu foil electrode showcases the characteristics of amorphous  $\text{SiO}_2$ , suggesting that the  $\text{SiO}_2$  network remains structurally stable and plays a critical role in accommodating volume changes during cycling. The absence of prominent peaks related to lithium–silicon alloy phases in all the three plots suggest that such phases are either non- crystalline or undergo structural loss after de-lithiation. Again, the presence of broad diffused background as displayed in the Fig.19 C shows the presence of amorphous phases, which might be attributed to the  $\text{Li}_x\text{Si}$  and surface solid-electrolyte interface layers formed during continuous lithiation and de-lithiation processes.

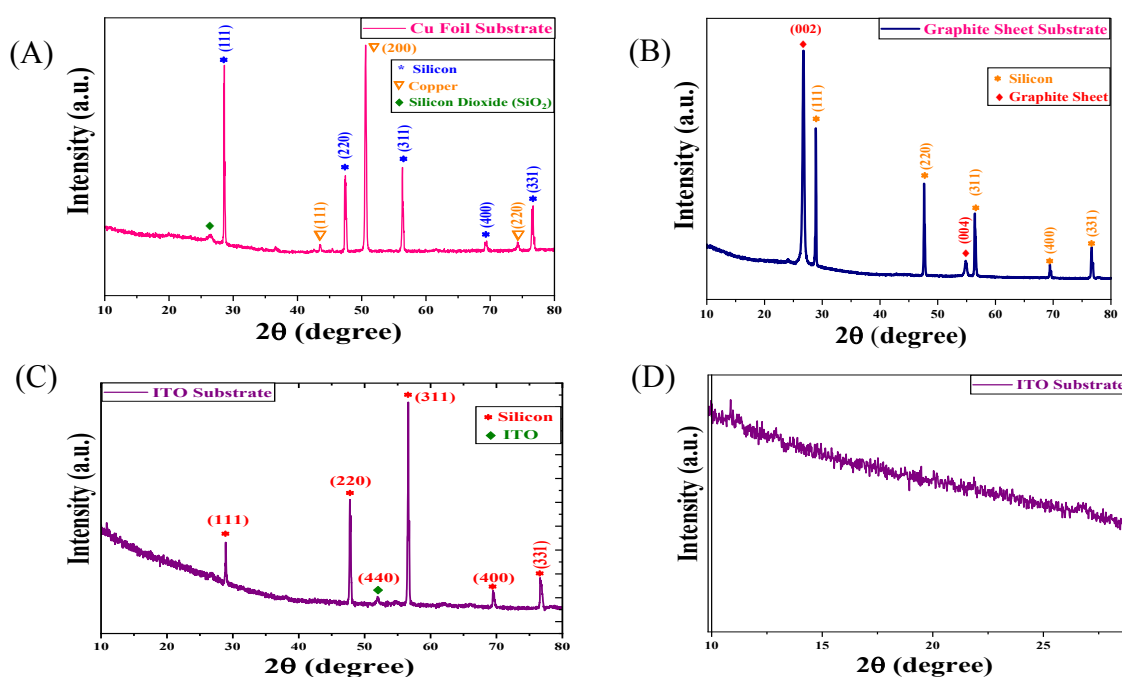


Fig. 19 X-ray diffraction (XRD) patterns of the recycled Si/SiO<sub>2</sub> composite electrodes deposited on different substrates after post-GCD (galvanostatic charge–discharge) cycling: (A) Cu foil substrate, (B) graphite sheet substrate, and (C) ITO substrate, (D) Plot showing the broad diffused background due to the presence of amorphous phases.

## 5 Conclusion

In summary, we have illustrated a simple and less – toxic approach of recycling of silicon solar cells for producing Si/SiO<sub>2</sub> composite powder. The recycled composite powder was found to have 99.52% purity value of silicon. This powder with the addition of CNTs and PVDF – NMP binder was then deposited over three different substrates which exhibited fine electrochemical performance with an appreciable reversible capacity. The electrochemical analysis also revealed distinct charge storage mechanisms for different current collectors. The electrodes prepared over copper foil and ITO showcased the characteristics of diffusion-controlled battery type behaviour, whereas the graphite substrate-based electrode indicated capacitive charge storage properties. Cyclic Voltammetry and electrical impedance spectroscopy measurements show good interfacial characteristics, while galvanometric charge discharge exhibited stable performance over 500 cycles. The specific capacitance values for deposited Cu foil, ITO and graphite sheet electrodes were calculated to be 143.23 Fg<sup>-1</sup>, 30.53 Fg<sup>-1</sup> and 163.92 Fg<sup>-1</sup> respectively. The close agreement between the fitted plot and experimental plots for electrodes prepared over different substrates show the reliability of the experimental results. Therefore, we found that the electrodes made over copper foil and ITO are applicable for silicon-based electrodes in Li – ion electrochemical systems, whereas the graphite substrate electrode can be a promising electrode in sustainability driven energy storage applications. Further work will focus on use of water-soluble binders, which allow environment friendly electrode fabrication along with enhancing the performance of the electrode by increasing cycling stability.

## Data availability

Data will be made available on request.

## Author contributions

Soumya Ranjan Nayak: experimental investigation, methodology, validation, formal analysis, data curation, writing – original draft, Manisha Balkhandia: data curation and formal analysis, Imran Chhimpia: data curation and formal analysis, Sushil Kumar: conceptualization,



visualization, validation, methodology, resources, supervision, data curation writing—review and editing. View Article Online  
DOI: 10.1039/D6SU00083E

## Conflicts of interest

There are no conflicts to declare.

## Acknowledgements

The authors are very thankful to the Director CSIR, National Physical Laboratory, New Delhi for his kind support. One of the authors, Soumya Ranjan Nayak, would like to acknowledge the University grants commission (UGC) Govt. of India for providing Senior Research Fellowship (SRF). The authors are thankful to Mr. Jai S. Tawale (CSIR-NPL) for FESEM characterization, Mr. Naval Kishore Upadhyaya for XRD characterization, Mr. Umesh Garnaik for Raman spectroscopy characterizations and Miss Ishika Aggarwal for the GCD characterizations.

## References

- 1 W. Akram, S. Salim, A. A. Al-Ghamdi, A. M. Kannan, A. Ahmed and H. Al-Salih, A review of life cycle assessment and sustainability analysis of photovoltaic recycling and disposal, *RSC Sustainability*, 2025, **3**, 21-36.
- 2 G. Wei, Y. Zhou, Z. Hou, Y. Li, Q. Liu, J. Chen and D. He, *Review of c-Si PV module recycling and industrial feasibility*, *EES Solar*, 2025, **1**, 9-29.
- 3 Rong Deng, Pablo Ribeiro Dias, Marina Monteiro Lunardi and Jingjia Ji, A sustainable chemical process to recycle end-of-life silicon solar cells, *Green Chem.*, 2021, **23**, 10157–10167.
- 4 S. Kim, J. Kim, S. Cho, K. Seo, Byoung-Uk Park, Hae-Seok Lee and J. Park, Development of eco-friendly pretreatment processes for high-purity silicon recovery from end-of-life photovoltaic modules, *RSC Adv.*, 2024, **14**, 31451–31460.
- 5 J. Park and N. Park, Wet etching processes for recycling crystalline silicon solar cells from end-of-life photovoltaic modules, *RSC Advances*, 2014, **4**, 34823–34829.
- 6 Huaixiang Yang, Yan Li, Weinan Chen, Chentong Zhang, Liuqing Huang and Xuetao Luo, Scalable synthesis of a Si/C composite derived from photovoltaic silicon kerf waste toward anodes for high-performance lithium-ion batteries. *ACS Energy & Fuels*, 2024, **38** (6), 5121–5130.



- 7 J. Qiu, C. Zhu, B. Ge, Y. Wang, Z. Zhang, J. Han, P. Shi, Y. Liu, Manufacturing lithium-ion anodes from silicon recovered from end-of-life solar panels, *Applied Surface Science*, 2025, **682**, 161605. View Article Online  
DOI: 10.1039/D5SU00083E
- 8 Global Market Outlook for Solar Power 2025-2029, 6 May 2025 <https://www.solarpowereurope.org/insights/outlooks/global-market-outlook-for-solar-power-2025-2029/detail>
- 9 Flavia C.S.M. Padoan, P. Altimari, F. Pagnanelli, Recycling of end-of-life photovoltaic panels: a chemical perspective on process development, *Solar Energy*, 2019, **177**, 746–761.
- 10 Physical Achievements, Installed Solar Power Energy Capacity as of 31<sup>st</sup> December, 2025.
- 11 S. Weckend, A. Wade and G. Heath, *End-of-life management: solar photovoltaic panels*, 2016, International Renewable Energy Agency (IRENA) and International Energy Agency Photovoltaic Power Systems Programme (IEA PVPS).
- 12 [www.irena.org](http://www.irena.org) (Report 26 March 2025)
- 13 M. Mottaghi, A. Kulkarni and J. M. Pearce, Recycling silicon photovoltaic cells into silicon anodes for Li-ion batteries using 3D printing, *RSC Sustainability*, 2025, **3**, 1859-1869,
- 14 Xiao-Bin Zhong, Yue-Xian Song, Yao-Hui Zhang, Yan-Gang Zhang, Xiao-Gang You, Pu-Guang Ji, Kurbanov Mirtemir Shodievich, Umedjon Khalilov, Gong-Kai Wang, Xin Zhang, Xing-Liang Yao, Feng Li, Jun-Fei Liang and Hua Wang, Regeneration of photovoltaic industry silicon waste toward high-performance lithium-ion battery anode, *Rare Metals*, 2024, **43(10)**, 4948- 4960.
- 15 Z. Dong, J. Li, P. Ge and Y. Yang, Upcycling of long-term Si/C composites by introducing interfacial chemical bonds from spent solar photovoltaic and lithium-ion batteries, *Green Chemistry*, 2025, **27**, 11914.
- 16 Z. Zhang, N. Yang, F. Xi, X. Chen, S. Li, W. Ma, Y. Lei and R. Deng, Purification of silicon from waste photovoltaic cells and its value-added application in lithium-ion batteries, *New Journal of Chemistry*, 2022, **46**, 11788.
- 17 H. Ji, J. Li, S. Li, Y. Cui, Z. Liu, M. Huang, C. Xu, G. Li, Y. Zhao and H. Li, High-Value Utilization of Silicon Cutting Waste and Excrementum Bombycis to Synthesize Silicon–Carbon Composites as Anode Materials for Li-Ion Batteries, *Nanomaterials*, 2022, **12(16)**, 2875.



- 18 O. Wang, Z. Chen and X. Ma, Advancing sustainable end-of-life strategies for photovoltaic modules with silicon reclamation for lithium-ion battery anodes, *Green Chemistry*, 2024, **26**, 3688–3697. View Article Online  
DOI: 10.1039/D6SU00083E
- 19 H. Ji, Z. Liu, X. Li, J. Li, Z. Yan and K. Tang, Recycling Silicon Waste from Photovoltaic Industry to Prepare Yolk-Shell Si@void@C Anode Materials for Lithium ion batteries, *Processes*, 2023, **11(6)**, 1764 .
- 20 M. M. Rahman, A. Nelson, S. Mateti, Y. Chen and Qi Han, Photovoltaic Recycled Nano Silicon-Silica Based Anode to Enhance Lithium-Ion Battery Performance, *SSRN Electronic Journal*, 2024,
- 21 C. Zhang, J. Li, Y. Feng, G. Du, Y. Liu, Ying Wang, Yun Wang, Z. Wu, P. Yang, A. Nanjundan, K. Yang, X. Zhu, L. Zhang, Recycling silicon cutting waste from photovoltaic industry into high-performance anodes for lithium-ion batteries, *ACS Sustainable Chemistry & Engineering*, 2024, **12, 37**, 14099–14108
- 22 L. Shen, K. Sun, F. Xi, Z. Jiang, S. Li, Y. Wang, Z. Tong, J. Lu, W. Ma, M. A. Green, and X. Hao, Conversion of photovoltaic waste silicon into amorphous Si nanowires for lithium-ion battery anodes, *Energy Environ. Sci.*, 2025, **18**, 4348-4361.
- 23 M.R. Kaiser, Z. Han, J. Liang, S.-X. Dou, J. Wang, Lithium sulfide-based cathode for lithium-ion/sulphur battery: recent progress and challenges, *Energy storage materials*, 2019, **19**, pp. 1-15.
- 24 F. Dou, Y. Weng, Q. Wang, G. Chen, H. Liu, L. Shi and D. Zhang, In situ imaging analysis of the inhibition effect of functional coating on the volume expansion of silicon anodes, *Chem. Eng. J.*, 2021, **417**, 128122.
- 25 B. Chen, L. Chen, L. Zu, Y. Feng, Q. Su, C. Zhang, J. Yang, Zero-Strain High-Capacity Silicon/Carbon Anode Enabled by a MOF-Derived Space-Confined Single-Atom Catalytic Strategy for Lithium-Ion Batteries. *Adv. Mater.*, 2022, **34 (21)**, 2200894.
- 26 Y. Zhang, W. Yang, X. Liu, G. Ma, G. Hu, Z. Liu, R. Yu, D. Zhuang, J. Xu, D. Zhao, L. Mai, L. Zhou, Necklace-Structured Silicon Suboxide-Based Anode Materials with Multiple Carbon Networks for Stable Lithium Storage. *Adv. Funct. Mater.*, 2024, **34**, 2315680.
- 27 X. Fan, T. Cai, S. Wang, Z. Yang, W. Zhang, Carbon Nanotube-Reinforced Dual Carbon Stress-Buffering for Highly Stable Silicon Anode Material in Lithium-Ion Battery, *Small*, 2023, **19 (30)**, 2300431.



- 28 H. Kang, J. Ko, S. Song and Y. Yoon, Recent Progress in Utilizing Carbon Nanotubes and Graphene to Relieve Volume Expansion and Increase Electrical Conductivity of Si-Based Composite Anodes for Lithium-Ion Batteries, *Carbon*, 2024, **219**, 118800. View Article Online  
DOI: 10.1039/D3SU00083E
- 29 C. Zhu, J. Qiu, Y. Wang, S. Gong, Y. Min, Y. Liu Penghui Shi, Recycling Co and Li from spent lithium-ion batteries using the silicon of spent photovoltaic panels, *New J. Chem.*, 2025, **49**, 8675–8685.
- 30 O. Wang and X. Ma, Innovating the recycling of silicon-based solar panels with an eco-friendly alkaline leaching process, *Resources, Conservation and Recycling*, 2024, **vol. 211**, 107887.
- 31 D. Sah and S. Kumar, Experimental, cost and waste analysis of recycling process for crystalline silicon solar module, *Sol. Energy*, 2024, **273**, 112534.
- 32 D. Sah, Chitra, and S. Kumar, Recovery and analysis of valuable materials from a discarded crystalline silicon solar module, *Solar Energy Materials and Solar Cells*, 2022, **vol.246**, 111908.
- 33 Wen-Jen Lee and Yong-Han Chang, Growth without Post-annealing of Monoclinic VO<sub>2</sub> Thin Film by Atomic Layer Deposition Using VCl<sub>4</sub> as Precursor, *Coatings*, 2018, **8**, 431.
- 34 Sonika Kodan, Ashwani Kumar, Amit Sanger, Alisha Arora, V.K. Malik and Ramesh Chandra, Vertically aligned MoSe<sub>2</sub>-WS<sub>2</sub> nano worms heterojunction towards room temperature NO<sub>2</sub> gas sensors, *Sensors and Actuators: B. Chemical*, 2024, **407**, 135481.
- 35 Bushra Jabeen and Uzaira Rafique, Synthesis and Application of Metal Doped Silica Particles for Adsorptive Desulphurization of Fuels, *Environ. Eng. Res.*, 2014, **19(3)**, 205-214.
- 36 D. Sah, Chitra, N. Upadhyay, S. Muthiah and S. Kumar, Growth and analysis of polycrystalline silicon ingots using recycled silicon from waste solar module, *Solar Energy Materials & Solar Cells*, 2023, **261**, 112524.
- 37 Z. Yang, X. Gong, B. Wang, D. Yang, T. Fu and Y. Liu, Efficient in situ generation of H<sub>2</sub>O<sub>2</sub> by novel magnesium–carbon nanotube composites, *RSC Adv.*, 2018, **8**, 35179–35186.
- 38 S. Kim, S. Ha, J. Lee, Y. Jeon and J. Hong, Preparation of Silicon Oxide-Carbon Composite with Tailored Electrochemical Properties for Anode in Lithium-Ion Batteries, *Journal of Carbon Research*, 2023, **9**, 114.



- 39 H. Kim, S. Yeo, M. Kim, G. Lee, Advancing silicon-based Li-ion batteries: enhanced stability and performance through carbon-coated Si and rGO linkage, *J Mater Sci*, 2023, **58**, 13621–13634.
- 40 H. Wu, L. Zheng, J. Zhan, N. Du, W. Liu, J. Ma, L. Su and L. Wang, Recycling silicon-based industrial waste as sustainable sources of Si/SiO<sub>2</sub> composites for high-performance Li-ion battery anodes, *Journal of Power Sources*, 2020, **449**, 227513.
- 41 J. Sun, J. Jiang, Z. Xu, L. Su, X. Zou, C. Gao, Y. Cui, Z. Zhou, X. Wang, H. Pan, L. Cao, Design and development of a high-performance epoxidized polyvinyl alcohol/chitosan dual cross-linked composite binder for the effective suppression of Si anode volume expansion, *Journal of Power Sources*, 2025, **639**, 236670.
- 42 C. Chen, S. Lee, M. Cho, J. Kim and Y. Lee, Cross-Linked Chitosan as an Efficient Binder for Si Anode of Li-ion Batteries, *ACS applied materials and interfaces*, 2016, **8**, 4, 2658–2665.

View Article Online  
DOI: 10.1039/D5SU00083E



View Article Online  
DOI: 10.1039/D6SU00083E

Open Access Article. Published on 29 April 2026. Downloaded on 5/1/2026 3:08:16 AM.  
This article is licensed under a Creative Commons Attribution 3.0 Unported Licence.



RSC Sustainability Accepted Manuscript

## Data availability

Data will be made available on request.

